

# Quantum study of reactions of interest in the interstellar medium: $\text{H}_2 + \text{N}^+ \rightarrow \text{NH}^+ + \text{H}$

Daniel Félix González

Máster en Química Teórica y Modelización Computacional

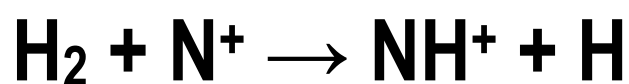


MÁSTERES  
DE LA UAM  
2021-2022

Facultad de Ciencias

# Master Erasmus Mundus in Theoretical Chemistry and Computational Modelling

## Quantum study of reactions of interest in the interstellar medium:



**Daniel Félix González**

Octavio Roncero Villa  
Alfredo Aguado Gómez



FACULTAD DE  
CIENCIAS

Autonomous University of Madrid (UAM) – Faculty of Science /  
Department of Applied Physical Chemistry

Master Thesis. Course 2021-2022

Quantum study of reactions of interest in the  
interstellar medium:  $\text{H}_2 + \text{N}^+ \longrightarrow \text{NH}^+ + \text{H}$

Daniel Félix González

# Contents

<b>1</b>	<b>Theoretical Introduction</b>	<b>6</b>
1.1	Reactions in the Interstellar Medium . . . . .	6
1.2	System Hamiltonian . . . . .	8
1.2.1	System Coordinates . . . . .	8
1.2.2	Kinetic Energy Operator . . . . .	11
1.2.3	Potential Energy Operator . . . . .	12
1.2.4	Total Wavefunction: Diabatic Basis Set . . . . .	13
1.2.5	Matrix elements . . . . .	17
1.3	Reaction Dynamics: Quantum Models . . . . .	19
1.3.1	Resonance-driven reactions . . . . .	21
1.3.2	Statistical method: Capture model . . . . .	22
<b>2</b>	<b>Methodology</b>	<b>23</b>
2.1	Numerical methods and Resonances . . . . .	23
2.1.1	One-dimensional model potential . . . . .	23
2.1.2	Discrete representations . . . . .	25
2.1.3	Numerov method . . . . .	26
2.1.4	Boundary conditions . . . . .	27
2.1.5	Numerical Propagation . . . . .	29
2.2	Time-independent approach . . . . .	30
2.2.1	Multi-dimensional potential and grids . . . . .	30
2.2.2	Given's method . . . . .	31
2.2.3	Numerov-Fox-Goodwin method . . . . .	31
2.2.4	Boundary conditions . . . . .	32
2.2.5	The 'aZticc' program . . . . .	33
2.3	Time-dependent validation . . . . .	37
2.3.1	The 'Madwave3' program . . . . .	37
<b>3</b>	<b>Results and Discussion</b>	<b>39</b>
3.1	One-dimensional problem . . . . .	39
3.1.1	Simulation parameters . . . . .	39

3.1.2	Analysis of the wavefunction and resonances . . . . .	40
3.2	Time-dependent method validation . . . . .	46
3.2.1	Simulation parameters . . . . .	47
3.2.2	Time-dependent convergence . . . . .	48
3.2.3	Validation of the statistical method . . . . .	49
3.3	Time-independent method . . . . .	54
3.3.1	Simulation parameters . . . . .	54
3.3.2	Analysis of the open and closed channels . . . . .	57
3.3.3	Analysis of the capture probabilities . . . . .	60
3.3.4	Truncation of the ro-vibrational basis . . . . .	63
3.3.5	Truncation of the helicity . . . . .	66
3.3.6	Analysis of the mass . . . . .	69
3.3.7	Further application of the method . . . . .	70

**4 Conclusions**

**75**

# Acknowledgements

This master thesis was supported by the UAM – TCCM scholarship of the Universidad Autónoma de Madrid (UAM).

I would like to dedicate this master thesis to my directors Octavio Roncero Villa and Alfredo Aguado Gómez, for their priceless support and assistance. Moreover, I am sincerely thankful for having provided me all the materials and help whenever it was needed. Special mention to professor Nadine Halberstadt from the University Toulouse III - Paul Sabatier, for her diligent and warm guidance during my internship in Toulouse.

# Abstract

In this master thesis, a detailed study of the reaction  $\text{N}^+(\text{}^3\text{P}_{J_A}) + \text{H}_2(\text{X}^1\Sigma_g^+) \longrightarrow \text{NH}^+(\text{X}^2\Pi, \text{}^4\Sigma) + \text{H}(\text{}^2\text{S})$  is performed. This reaction of astrochemical relevance not only serves as a model system for three-atom insertion reactions, but also allows to unveil the underlying principles of reactivity and quantum dynamics models. The formal derivation of the Hamiltonian of the system is presented, along with the construction of suitable *symmetry-adapted* basis functions that account for the asymptotic reactants and products arrangements. The concept of *resonance* is carefully explored, at first in a one-dimensional *Eckart potential* to analyse its general features, and afterwards applied to the actual system of study. The dynamic simulations of the reaction is made by means of a *statistical method*, with both *adiabatic* and *quantum* approaches, implemented in the program *aZticc* developed by the present research group. By comparison with accurate *time-dependent* wavepacket propagation methods, one concludes that the *statistical approach* is as a powerful *time-independent* alternative for reactions with a long-lived intermediate complex. An evaluation of the influence of the different simulation parameters on the results is then performed, such as the angular momenta or isotopic mass effects, and only considering a single *adiabatic* electronic potential energy surface (PES) for simplicity. Finally, an introduction to the quantitative determination of *reaction cross-sections* and *thermal rate-constants* is presented, this time considering *non-adiabatic* couplings between the different spin-orbit states of the system with an optimal set of PES.

# Resumen

En este trabajo de fin de máster, se lleva a cabo un estudio detallado de la reacción  $\text{N}^+(\text{}^3\text{P}_{J_A}) + \text{H}_2(\text{X}^1\Sigma_g^+) \longrightarrow \text{NH}^+(\text{X}^2\Pi, \text{}^4\Sigma) + \text{H}(\text{}^2\text{S})$ . Esta reacción de relevancia astroquímica no solo sirve como un sistema modelo para reacciones de inserción de tres átomos, sino que también permite desentrañar los principios subyacentes de los modelos de reactividad y dinámica cuántica. La derivación formal del Hamiltoniano del sistema es presentada, junto con la construcción de unas adecuadas funciones de base *adaptadas a la simetría* para los canales de reactivos y productos. El concepto de *resonancia* es explorado minuciosamente, inicialmente en un potencial de Eckart monodimensional para analizar sus características generales, y posteriormente aplicado al auténtico sistema de estudio. Las simulaciones dinámicas de la reacción se llevan a cabo mediante un método estadístico, tanto *adiabático* como *cuántico*, implementado en el programa *aZticc* desarrollado por el presente grupo de investigación. Al comparar con métodos precisos *dependientes del tiempo* de propagación de paquetes de onda, se concluye que el *método estadístico* es una poderosa alternativa *independiente del tiempo* para aquellas reacciones con un complejo intermedio duradero. A continuación, se evalúa la influencia de los distintos parámetros de simulación, como los momentos angulares o efectos isotópicos de la masa, y considerando solo una única superficie de energía potencial (PES) adiabática por simplicidad. Finalmente, se presenta una introducción a la determinación cuantitativa de *secciones eficaces* de reacción y *constantes cinéticas*, esta vez considerando acoplamientos *no adiabáticos* entre los diferentes estados espín-órbita del sistema con superficies PES óptimas.

# Chapter 1

## Theoretical Introduction

### 1.1 Reactions in the Interstellar Medium

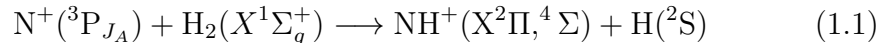
The study of the evolution of the abundances of molecular species allows the probe of physical conditions along the stellar evolution in space — from the parent molecular cloud to the star system, passing through intermediate stages such as cold and hot cores, or the protoplanetary disk.

Among the most abundant elements, nitrogen deserves a special consideration, because it predominately occurs in the form of  $\text{N}_2$  and atomic nitrogen — rather difficult to detect, specially in cold cores. For this reason, the abundance of nitrogen is established by other molecules as  $\text{NH}_n$ , CN, HCN/HNC or  $\text{N}_2\text{H}^+$ , which requires the construction of increasingly more accurate chemical networks [1,2]. Therefore, the formation of hydrides, the first step of the chemistry in space, is particularly important for the study of nitrogen in astrochemistry — in fact, ammonia was one of the first polyatomic molecules to be detected in the interstellar medium (ISM) [3].

In photodissociation regions (PDR), hydrides of more electropositive elements like O, C, S, are usually formed from the successive addition of hydrogen atoms to the element cation, followed by dissociative recombination with electrons. In spite of this, the ionization step of nitrogen hydrides is more difficult due to the larger ionization energy of nitrogen than hydrogen, unlike the more metallic elements — nitrogen hydrides present a comparatively smaller number of reactions in the chemical networks, with a smaller population of  $\text{N}^+$ . The alternative route to form nitrogen hydrides involves only neutral species — N with OH or CH [1].

The rate constants involved in the first steps of chemical networks have an enormous influence in the relative abundances, ortho/para ratios and

deuteration fractions of many nitrogen-containing molecules [4]. In consequence, numerous experiments have been performed to study the following reaction [5–8].



The main problem is that the experiments are in different conditions, so the exact thermalization conditions of the reaction are unknown, and an analysis on the influence of the fine structure of  $\text{N}^+(\text{}^3\text{P}_{J_A})$  is needed.

Various theoretical attempts to characterize this reaction have already been made [9–11], involving dynamical calculations on the ground adiabatic electronic state potential, but ignoring the fine structure of nitrogen — with both classical [11, 12] and quantum approaches [13, 14]. Although these studies did not completely solve the problem, they have revealed important features about this reaction. For instance, the reaction dynamics of the ground adiabatic state is mediated by many long-lived resonances because of the presence of a deep insertion well in the potential energy surface (PES). This suggests that the reaction may proceed statistically, and the latest models focus on this assumption [15, 16].

The main goal of this work is to study in detail the already mentioned reaction of astrochemical interest — nitrogen cation hydrogenation — from a theoretical point of view, as a model example of *insertion reactions* with a deep well.

A formal derivation of the *thermal rate constant*  $k(T)$  —naturally arising from the *reaction cross-section*  $\sigma$  — will be presented through this study. It starts from the definition of the Hamiltonian operator for a *body-fixed* Jacobi coordinate system, followed by general aspects of the *ab initio* calculation of the electronic *Potential Energy Surface* (PES) and its *diabatization* procedure for *non-adiabatic* dynamical studies.

Finally, the focus is placed on the estimation of the *reaction cross section* within the statistical *quantum capture* model —solving the *close-coupling* equations—. The validity of this approach is carefully explored by introducing the concept of *resonance*, and a comparison with the standard *time-dependent* wavepacket propagation method will prove it to be a powerful alternative to the latter.

## 1.2 System Hamiltonian

### 1.2.1 System Coordinates

The system of interest,  $\text{NH}_2^+$ , has three atoms, which implies a total number of 9 nuclear degrees of freedom —the electronic coordinates, which have to refer as well to the nuclear coordinates, are collectively treated separately in an electronic Hamiltonian (unlike the standard Born-Oppenheimer approximation, for which they are treated implicitly within the potential). In a generic *space-fixed* frame, these can be accounted by the three-dimensional Cartesian coordinates of each atom:

$$\vec{r}_N^{sf} = \begin{pmatrix} x_N^{sf} \\ y_N^{sf} \\ z_N^{sf} \end{pmatrix} \quad \vec{r}_{H_A}^{sf} = \begin{pmatrix} x_{H_A}^{sf} \\ y_{H_A}^{sf} \\ z_{H_A}^{sf} \end{pmatrix} \quad \vec{r}_{H_B}^{sf} = \begin{pmatrix} x_{H_B}^{sf} \\ y_{H_B}^{sf} \\ z_{H_B}^{sf} \end{pmatrix} \quad (1.2)$$

It is useful to factor out the motion of the Center of Mass of the total system  $\vec{R}_{CM}$  —which only matters for a global translation of the whole system— and focus on the six relative internal degrees of freedom.

$$\vec{R}_{CM}^{sf} = \sum_a \frac{m_a}{M} \vec{r}_a^{sf} \quad \text{with} \quad M = \sum_a m_a \quad (1.3)$$

For convenience, the remaining internal degrees of freedom can be easily expressed in terms of Jacobi coordinates [17]. To do that, it is essential to understand the system as a diatomic molecule with an atom ( $A + \text{BC}$ ).

Depending on the actual diatomic and atomic fragments considered, there are three possibilities: (a)  $\text{H}_2 + \text{N}^+$ , (b)  $\text{NH}_A^+ + \text{H}_B$  or (c)  $\text{NH}_B^+ + \text{H}_A$ . However, since  $\text{H}_A$  and  $\text{H}_B$  are chemically identical, possibilities (b) and (c) are equivalent. From now on, (a) will be denoted as the *reactant arrangement*, while both (b) and (c) will be the *product arrangement* — see Figure 1.1.

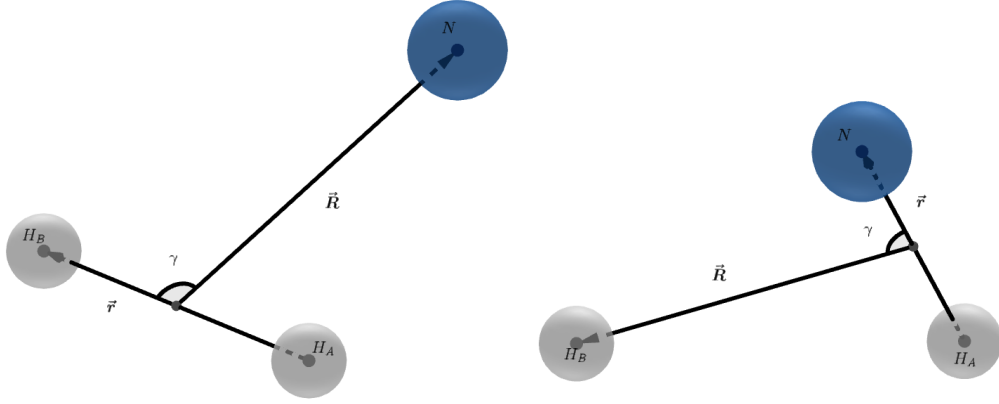


Figure 1.1: Jacobi Coordinates of the reactant arrangement  $\text{H}_2 + \text{N}^+$  (left) and product arrangement  $\text{NH}^+ + \text{H}$  (right)

In general, the internal nuclear vector coordinates are chosen as  $\vec{R}$  (from the atom to the center of mass of the diatom) and  $\vec{r}$  (internal vector of the diatomic fragment), both expressed in spherical coordinates [18].

$$\vec{R} = \begin{pmatrix} R \sin \theta \cos \phi \\ R \sin \theta \sin \phi \\ R \cos \theta \end{pmatrix} \quad \vec{r} = \begin{pmatrix} r \sin \gamma \cos \chi \\ r \sin \gamma \sin \chi \\ r \cos \gamma \end{pmatrix} \quad (1.4)$$

Although there are six scalar internal coordinates to consider, three of them can be identified with the effect of rotations on the whole system ( $\phi$ ,  $\theta$ ,  $\chi$ ). These three angular coordinates are the well-known *Euler Angles* [19] (as seen in Figure 1.2), and their net effect can be parametrized by a general spatial rotation matrix  $\mathfrak{R}(\phi, \theta, \chi)$  —product of three successive rotations.

$$\mathfrak{R}(\phi, \theta, \chi) = \mathfrak{R}_{z''}(\chi) \mathfrak{R}_{y'}(\theta) \mathfrak{R}_z(\phi) \quad (1.5)$$

$$\mathfrak{R}_{z''}(\chi) = \begin{pmatrix} \cos \chi & \sin \chi & 0 \\ -\sin \chi & \cos \chi & 0 \\ 0 & 0 & 1 \end{pmatrix}$$

$$\mathfrak{R}_{y'}(\theta) = \begin{pmatrix} \cos \theta & 0 & -\sin \theta \\ 0 & 1 & 0 \\ \sin \theta & 0 & \cos \theta \end{pmatrix}$$

$$\mathfrak{R}_z(\phi) = \begin{pmatrix} \cos \phi & \sin \phi & 0 \\ -\sin \phi & \cos \phi & 0 \\ 0 & 0 & 1 \end{pmatrix}$$

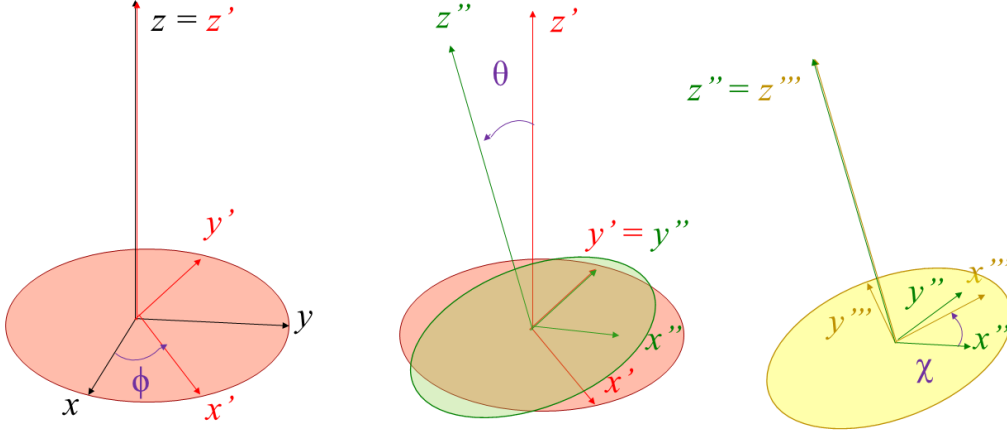


Figure 1.2: Schematic effect of the three Euler angles  $\phi$ ,  $\theta$ ,  $\chi$ .

The application of the rotation matrix allows us to define a new rotating *body-fixed* frame to which all the vectors are referred—for convenience,  $\vec{R}$  is aligned with the *body-fixed* z-axis. For the Cartesian expressions of  $\vec{R}$  and  $\vec{r}$ , the relationship between both frames is given by the following relations.

$$\vec{R}^{bf} = \mathfrak{R}(\phi, \theta, \chi) \vec{R}^{sf} \quad \vec{r}^{bf} = \mathfrak{R}(\phi, \theta, \chi) \vec{r}^{sf} \quad (1.6)$$

As a consequence, there are only three degrees of freedom left to specify,  $\{R, r, \gamma\}$ , which will be the actual internal coordinates to refer to in this study.

Finally, for each vector coordinate it is possible to define a reduced mass and recast them as a mass-scaled coordinates. In the general case of A + BC, these are given by the following expressions.

$$\tilde{R} = R\sqrt{\mu} \quad \mu = \left( \frac{1}{m_A} + \frac{1}{m_B + m_C} \right)^{-1} \quad (1.7)$$

$$\tilde{r} = r\sqrt{\mu_{BC}} \quad \mu_{BC} = \left( \frac{1}{m_B} + \frac{1}{m_C} \right)^{-1} \quad (1.8)$$

Using this new formulation, it is possible to define for each vector coordinate an associated angular momentum operator, which will be useful for the final construction of the Hamiltonian operator.

$$\vec{\ell} = -i\hbar \vec{R} \times \vec{\nabla}_{\tilde{R}} \quad \vec{j} = -i\hbar \vec{r} \times \vec{\nabla}_{\tilde{r}} \quad (1.9)$$

Up to now, all the coordinate definitions have been limited to the motion of the three nuclei, completely neglecting the presence of the electrons of the system —as it is expected for the ordinary Born-Oppenheimer approximation. However, the angular momentum arising from the electrons, as well as non-adiabatic features of the electronic motion are of great significance, hence they will be explicitly covered while describing the electronic potential of the system.

### 1.2.2 Kinetic Energy Operator

The *total kinetic energy* operator  $\hat{T}$  is factored into a *translational kinetic energy*  $\hat{T}_{CM}$  and an *internal kinetic energy* operator  $\hat{T}_{int}$ . The latter describes the motion of the molecule regardless global translations, and thus is the most important one.

$$\hat{T} = \hat{T}_{CM} + \hat{T}_{int} \quad \hat{T}_{int} = -\frac{\hbar^2}{2}\nabla^2 \quad (1.10)$$

$$\nabla^2 = \sum_{\alpha,\beta} \frac{1}{\sqrt{|g|}} \frac{\partial}{\partial q^\alpha} \left( \sqrt{|g|} g_{\alpha,\beta}^{-1} \frac{\partial}{\partial q^\beta} \right)$$

The total internal Laplacian ( $\nabla^2$ ) is obtained from the partial derivatives of all the internal coordinates, weighted by the metric matrix  $g$  associated to the algebraic space spanned by the generalized mass-scaled coordinates ( $q^\alpha, q^\beta$ ).

Following the rigorous construction of the Laplacian operator [17], it is possible to rewrite the internal kinetic energy operator as a purely radial-dependent part  $\hat{T}_{rad}$  (dependent of  $R, r$ ) and an angular part  $\hat{T}_{ang}$  (related to the angular momenta of each coordinate). If the electronic degrees of freedom are neglected and taken apart in their own operator, the expression of the internal kinetic energy operator, expressed in Jacobi coordinates, has the following form.

$$\hat{T}_{int} = \hat{T}_{rad} + \hat{T}_{ang} \quad (1.11)$$

$$\hat{T}_{rad} = -\frac{\hbar^2}{2\mu} \left( \frac{2}{R} \frac{\partial}{\partial R} + \frac{\partial^2}{\partial R^2} \right) - \frac{\hbar^2}{2\mu_{BC}} \left( \frac{2}{r} \frac{\partial}{\partial r} + \frac{\partial^2}{\partial r^2} \right)$$

$$\hat{T}_{ang} = \frac{\ell^2}{2\mu R^2} + \frac{j^2}{2\mu_{BC} r^2}$$

### 1.2.3 Potential Energy Operator

Following the Born-Oppenheimer approximation, the total internal Hamiltonian  $\hat{H}$  is separated into a nuclear term  $\hat{H}_{nuc}$  and an electronic potential term  $\hat{H}_{el}^{tot}$ .

$$\hat{H} = \hat{H}_{nuc} + \hat{H}_{el}^{tot} \quad \hat{H}_{nuc} \equiv \hat{T}_{int} \quad \hat{H}_{el}^{tot} \equiv \hat{V} \quad (1.12)$$

The nuclear motion is already described by the previous section (kinetic energy operator), which implies that there is only left the detailed specification of the total electronic Hamiltonian (potential energy operator). The total electronic Hamiltonian operator can be decomposed into the *non-relativistic electronic Hamiltonian*  $\hat{H}_{el}$  and the *spin-orbit Hamiltonian*  $\hat{H}_{SO}$ .

$$\hat{V} = \hat{H}_{el} + \hat{H}_{SO} \quad (1.13)$$

The non-relativistic electronic Hamiltonian can be better described by a perturbative decomposition [20], where the zero-order term  $\hat{H}_{el}^0$  corresponds to the asymptotic limit of separated atom  $A$  and diatomic  $BC$  fragments ( $R \rightarrow \infty$ ), and the perturbation  $\hat{H}_{el}^1$  is just the interaction of both fragments.

$$\hat{H}_{el} = \hat{H}_{el}^0 + \hat{H}_{el}^1 \quad (1.14)$$

The explicit form of the electronic potential operator with its matrix elements is detailed in section 2.2.5.

#### Electronic angular momentum contribution

The derivation of the purely nuclear kinetic energy terms shown in section 1.2.2 only account for the angular momenta originated from the motion of the nuclei alone — *i.e.* structureless point masses *a priori*. However, the electronic motion does indeed contribute to the total angular momentum of the whole system. For this reason, it is important to recast the angular momenta used in the previous equations to include the electronic angular momenta for the subsequent definition of meaningful basis functions [17].

In general, the angular momentum operator  $\vec{j}$  is associated to the diatomic fragment  $BC$  asymptotically, so it can be decomposed into the rotational angular momentum arising from the motion of the diatomic nuclei  $\vec{N}$ , plus the total electronic angular momentum of the diatom  $\vec{j}_e$  —the sum of the

diatomic orbital angular momentum  $\vec{L}_{BC}$  and spin  $\vec{S}_{BC}$ — with a total projections on the body-fixed diatomic internuclear axis  $\Omega_{BC}$  (of  $\vec{j}_e$ ),  $\Lambda_{BC}$  (of  $\vec{L}_{BC}$ ) and  $\Sigma_{BC}$  (of  $\vec{S}_{BC}$ ).

$$\vec{j} = \vec{N} + \vec{j}_e \quad \vec{j}_e = \vec{L}_{BC} + \vec{S}_{BC} \quad \Omega_{BC} = \Lambda_{BC} + \Sigma_{BC} \quad (1.15)$$

On the other hand, although the atomic fragment  $A$  has not nuclear rotation contribution, it has an asymptotically defined total electronic angular momentum  $\vec{J}_A$ —sum of the atomic orbital angular momentum  $\vec{L}_A$  and spin  $\vec{S}_A$ —, with a total projection on the *body-fixed* z-axis  $\Omega_A$  (of  $\vec{J}_A$ ),  $\Lambda_A$  (of  $\vec{L}_A$ ) and  $\Sigma_A$  (of  $\vec{S}_A$ ).

$$\vec{J}_A = \vec{L}_A + \vec{S}_A \quad \Omega_A = \Lambda_A + \Sigma_A \quad (1.16)$$

If the nuclear spin angular momentum is neglected, the total angular momentum of the system  $\vec{J}$  can be asymptotically (for  $R \rightarrow \infty$ ) be written as the sum of all the previously mentioned angular momenta.

$$\vec{J} = \vec{\ell} + \vec{j} + \vec{J}_A \quad (1.17)$$

Analogously, the projection of  $\vec{J}$  on the z-axis are respectively  $M$  (*space-fixed*) and  $\Omega$  (*body fixed*).

Recalling the actual system of study, the final angular momenta to consider are slightly easier to treat than the general case. For instance, in the *reactant arrangement*, the diatomic fragment  $H_2(X \ ^1\Sigma^+)$  has no electronic angular momentum ( $j_e = 0$ ), so  $j$  only comes from the rotational contribution.

#### 1.2.4 Total Wavefunction: Diabatic Basis Set

According to the postulates of quantum mechanics [21], the whole system can be described by a total wavefunction  $\Psi$ —which is *a priori* unknown in its exact form. However, what really matters from a practical point of view are the energy eigenstates of the system  $\Psi_E$ , which have a well-defined energy—*i.e.* eigenfunctions of the Hamiltonian operator—. Since this system involves the dynamical motion of all atoms in reactive collisional events, the energy eigenfunction spectrum is expected to form a continuum, being the definite energy  $E$  one of the few labels to characterize each of the eigenstates. In order to properly obtain as much information as possible for each state, it is required to find those operators which commute with the Hamiltonian and adopt their well-defined eigenvalues as additional labels for the wavefunction.

This is the case of the Total Angular Momentum  $J$ , which is conserved for isolated systems by definition, as well as the symmetry operators—in case of having any point symmetry. Additionally, given that the total angular momentum has a well-defined value  $J$ , its z-axis projections  $M$  (*space-fixed*) or  $\Omega$  (*body-fixed*) can also take definite values, since operators  $\hat{J}^2$  and  $\hat{J}_z$  commute to each other [19, 21]—though not invariant, as they depend on the actual rotational configuration of the system ( $\Omega$  is not conserved). This leaves us with a total nuclear wavefunction labelled as  $\Psi_E^J(R, r, \gamma, \phi, \theta, \chi)$  which results from a linear combination of all the possible  $\Omega$  values of the system ( $\Omega = 0, \pm 1, \dots, \pm J$ ).

The next suitable step is to represent the wavefunction  $\Psi_E^J$  by two radial-dependent functions  $\Phi(R)$ ,  $\varphi(r)$  and another purely angular-dependent function denoted as  $\mathcal{W}(\gamma, \phi, \theta, \chi)$ . This separation is possible due to the unique properties of the Jacobi coordinates [17]—note that it is not the case of the electronic coordinates, which are implicit variables for all the three functions, but omitted for convenience.

$$\Psi_E^J(R, r, \gamma, \phi, \theta, \chi) = \sum_{\Omega} \frac{\Phi(R)}{R} \frac{\varphi(r)}{r} \mathcal{W}^{J\Omega}(\gamma, \phi, \theta, \chi) \quad (1.18)$$

It is worth to mention that each radial-dependent function is divided by its own coordinate in order to simplify the expression of the radial matrix elements of the Hamiltonian—the Jacobian reduces from  $R^2 dR$  to simply  $dR$ .

Up to now, the wavefunction is general and applicable for all three-atom systems. However, it is even more important to consider the asymptotic limit for independent atom  $A$  and diatom  $BC$  fragments, because it plays a fundamental role in the final identification of the reactant and product arrangements—the final objective of this study after all. For this reason, it is useful to rewrite the total wavefunction in terms of asymptotically well-defined observables, briefly described below.

The atomic electronic angular momentum  $J_A$  with its projection  $\Omega_A$  only contribute to the angular part of the wavefunction, so their associated eigenfunction  $|J_A \Omega_A\rangle$  is included in  $\mathcal{W}^{J\Omega}$ . Conversely, the diatomic rotational angular momentum  $j$  has a certain contribution in the  $r$ -dependent function too. Hence,  $\varphi(r)$  is identified as the diatomic rovibrational eigenfunctions of the diatomic fragment  $\varphi_{jv}(r)$ —with a vibrational quantum number  $v$ . Taking this new asymptotic basis [17], the final expansion of the wavefunction

becomes a superposition of all possible channels —collectively denoted with the global quantum number  $\alpha \equiv \{\Omega, J_A, \Omega_A, j, v\}$ .

$$\Psi_E^J(R, r, \gamma, \phi, \theta, \chi) = \sum_{\alpha} \frac{\Phi_{\alpha}(R)}{R} \frac{\varphi_{jv}(r)}{r} \mathcal{W}_{jJ_A\Omega_A}^{J\Omega}(\gamma, \phi, \theta, \chi) \quad (1.19)$$

Of course, the *body-fixed* angular function  $\mathcal{W}_{jJ_A\Omega_A}^{J\Omega}$  can be related to its *space-fixed* counterpart  $\mathcal{Y}_{jJ_A\Omega_A}^{JM}$  taking into account the effect of the rotations of the three Euler angles. This is achieved via *Wigner's rotation matrices*  $\mathcal{D}_{M\Omega}^J(\phi, \theta, \chi)$  [19, 22] — factorizable in individual rotation matrices  $e^{-iM\phi}$ ,  $d_{M\Omega}^J(\theta)$  and  $e^{-i\Omega\chi}$ .

$$\begin{aligned} \mathcal{W}_{jJ_A\Omega_A}^{J\Omega}(\gamma, \phi, \theta, \chi) &= \sqrt{\frac{2J+1}{8\pi^2}} \mathcal{D}_{M\Omega}^{J*}(\phi, \theta, \chi) \mathcal{Y}_{jJ_A\Omega_A}^{JM}(\gamma, 0) \quad (1.20) \\ \mathcal{D}_{M\Omega}^J(\phi, \theta, \chi) &\equiv e^{-iM\phi} d_{M\Omega}^J(\theta) e^{-i\Omega\chi} \end{aligned}$$

Where  $\mathcal{Y}_{jJ_A\Omega_A}^{JM}$  is just the product of the atomic electronic eigenfunction  $|J_A\Omega_A\rangle$  and the *space-fixed* spherical harmonics of the diatomic fragment  $Y_{j\lambda}$ .

$$\mathcal{Y}_{jJ_A\Omega_A}^{JM}(\gamma, 0) = Y_{j\lambda}(\gamma, 0) |J_A\Omega_A\rangle \quad (1.21)$$

As a matter of nomenclature, the *body-fixed* angular basis  $\mathcal{W}_{jJ_A\Omega_A}^{J\Omega}$  is finally written as  $|J\Omega j J_A\Omega_A\rangle$ .

The only last consideration to take into account for the definition of the wavefunction is the presence of symmetries in the system. In three-atom systems such as the one of this study,  $\text{NH}_2^+$ , there is a symmetry plane operator  $\hat{\sigma}_{xz}$  which is expected for the *body-fixed* frame. Conceptually, this *body-fixed symmetry plane* is a natural consequence of the *space-fixed inversion operator*  $\mathcal{E}^*$  [17].

$$\mathcal{E}^*(R, \theta, \phi) \rightarrow (R, \pi - \theta, \phi + \pi) \quad \mathcal{E}^*(r, \gamma, \chi) \rightarrow (r, \gamma, \pi - \phi) \quad (1.22)$$

$$\mathcal{E}^* |J\Omega j J_A\Omega_A\rangle = (-1)^{J+J_A+L} |J - \Omega j J_A - \Omega_A\rangle$$

In order to make the angular basis functions to be eigenfunctions of the inversion operator, it is only required to take linear combinations of the predefined basis functions [17].

$$|J\Omega j J_A \Omega_A p\rangle = c_{\Omega\Omega_A} [|J\Omega j J_A \Omega_A\rangle + p(-1)^{J+J_A+L} |J - \Omega j J_A - \Omega_A\rangle] \quad (1.23)$$

$$c_{\Omega\Omega_A} = \sqrt{\frac{2 - \delta_{0\Omega}\delta_{0\Omega_A}}{4}} \quad p = \pm 1$$

This way, there are two main families of functions depending on their *parity* eigenvalue  $p = \pm 1$ .

$$\mathcal{E}^* |J\Omega j J_A \Omega_A p\rangle = p |J\Omega j J_A \Omega_A p\rangle \quad (1.24)$$

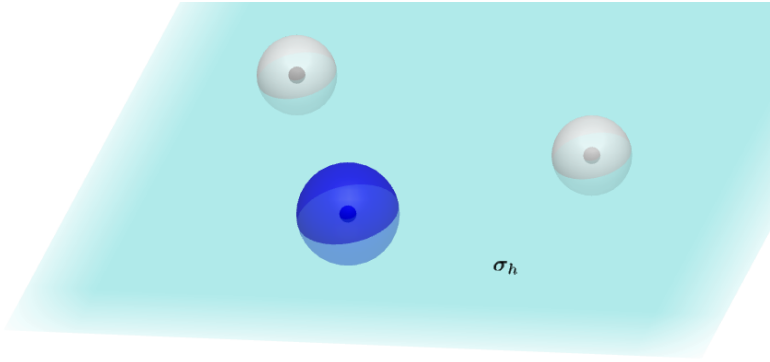


Figure 1.3: Symmetry plane of the system in the body-fixed frame

With all these considerations, the *adiabatic* basis functions are fully characterized for any arbitrary three-atom system.

The nuclear spin has been neglected systematically during the present derivations, since its effect is assumed to be reasonably small in general. However, in the system of study  $\text{NH}_2^+$ , in the *reactant arrangement*, there is the diatomic molecule  $\text{H}_2$ , which is strongly affected by its nuclear spin — it is possible to distinguish between the nuclear triplet state o- $\text{H}_2$  (ortho hydrogen) and the nuclear singlet p- $\text{H}_2$  (para hydrogen) [23, 24]. Taking into account the permutational symmetry of the two identical hydrogen atoms, the o- $\text{H}_2$  corresponds to symmetric nuclear spin functions ( $|\uparrow\uparrow\rangle, |\downarrow\downarrow\rangle, \frac{1}{\sqrt{2}} [|\uparrow\downarrow\rangle + |\downarrow\uparrow\rangle]$ ) and p- $\text{H}_2$  to antisymmetric nuclear spin functions ( $\frac{1}{\sqrt{2}} [|\uparrow\downarrow\rangle - |\downarrow\uparrow\rangle]$ ).

The two possible *spin isomers* of hydrogen have significant implications in the final allowed values of the diatomic angular momentum  $j$  [24]. The two hydrogen nuclei are particles of spin  $I = \frac{1}{2}$ , subject to the usual permutational antisymmetry requirement of fermions for the diatomic wavefunction [21].

For that reason, recalling the permutational symmetry of the two nuclear spin isomers, we conclude that the o-H<sub>2</sub> only has odd  $j$  values, while p-H<sub>2</sub> is restricted to even  $j$  values.

Of course, this additional *diatomic parity* restriction only applies to the *reactant arrangement* with H<sub>2</sub>, but not for the *product arrangements* — nor for a general ABC system.

### 1.2.5 Matrix elements

Once the wavefunction is completely defined, there is only left to evaluate the matrix form of the Hamiltonian operator in the chosen basis set.

$$\begin{aligned} \hat{H}_{int} &= -\frac{\hbar^2}{2\mu} \left( \frac{2}{R} \frac{\partial}{\partial R} + \frac{\partial^2}{\partial R^2} \right) - \frac{\hbar^2}{2\mu_{BC}} \left( \frac{2}{r} \frac{\partial}{\partial r} + \frac{\partial^2}{\partial r^2} \right) \\ &\quad + \frac{\ell^2}{2\mu R^2} + \frac{j^2}{2\mu_{BC} r^2} + \hat{H}_{el} + \hat{H}_{SO} \\ \Psi_E^J &= \sum_{\alpha} \frac{\Phi_{\alpha}(R)}{R} \frac{\varphi_{jv}(r)}{r} |J\Omega j J_A \Omega_A p\rangle \end{aligned} \quad (1.25)$$

#### Radial Elements

The radial functions  $\Phi_{\alpha}(R)$  are initially unknown, since they depend on all the quantum numbers of each function of the diabatic basis set. As a consequence, they are numerically obtained in the resolution of the *close-coupling* equations [25–27], which will be properly described later in the next sections.

$$-\frac{\hbar^2}{2\mu} \left\langle \frac{\Phi_{\alpha'}}{R} \left| \left( \frac{2}{R} \frac{\partial}{\partial R} + \frac{\partial^2}{\partial R^2} \right) \right| \frac{\Phi_{\alpha}}{R} \right\rangle = -\frac{\hbar^2}{2\mu R^2} \langle \Phi_{\alpha'} | \frac{\partial^2}{\partial R^2} | \Phi_{\alpha} \rangle \quad (1.26)$$

On the other hand, the diatomic radial functions  $\varphi_{jv}(r)$  are easy to obtain numerically, by application of the standard procedures for diatomic molecules — see section 2.2.2.

$$-\frac{\hbar^2}{2\mu_{BC}} \left\langle \frac{\varphi_{j'v'}}{r} \left| \left( \frac{2}{r} \frac{\partial}{\partial r} + \frac{\partial^2}{\partial r^2} \right) \right| \frac{\varphi_{jv}}{r} \right\rangle = -\frac{\hbar^2}{2\mu_{BC} r^2} \langle \varphi_{j'v'} | \frac{\partial^2}{\partial r^2} | \varphi_{jv} \rangle \quad (1.27)$$

## Angular Elements

The angular Elements of the Hamiltonian are relatively simple to obtain, since the selected angular basis is defined to include the eigenfunctions of the angular momentum operators — as shown by *Jouvet et al.* [20].

$$\frac{1}{2\mu_{BC}r^2} \langle J\Omega' j' J'_A \Omega'_A p | j^2 | J\Omega j J_A \Omega_{AP} \rangle \Rightarrow \langle Y_{j'\lambda'} | j^2 | Y_{j\lambda} \rangle = \hbar^2 j(j+1) \delta_{jj'} \delta_{\lambda\lambda'} \quad (1.28)$$

For the angular momentum associated to  $R$ , the same deductions are made if its expression in terms of the total angular momentum is written.

$$\frac{1}{2\mu R^2} \langle J\Omega' j' J'_A \Omega'_A p | \ell^2 | J\Omega j J_A \Omega_{AP} \rangle \quad (1.29)$$

For the special case of the angular momentum  $\vec{\ell}$ , it is usually preferred to replace it in terms of the total angular momentum  $\vec{J}$ .

$$\begin{aligned} \vec{J} = \vec{\ell} + \vec{j} + \vec{J}_A &\Rightarrow \vec{\ell} = \vec{J} - \vec{j} - \vec{J}_A & (1.30) \\ \ell^2 = J^2 + j^2 + J_A^2 - 2(\vec{J} \cdot \vec{j} + \vec{J} \cdot \vec{J}_A - \vec{j} \cdot \vec{J}_A) &\Rightarrow \\ \langle J\Omega' j' J'_A \Omega'_A | J^2 | J\Omega j J_A \Omega_A \rangle &= \hbar^2 J(J+1) \delta_{\Omega\Omega'} \\ \langle Y_{j'\lambda'} | j^2 | Y_{j\lambda} \rangle &= \hbar^2 j(j+1) \delta_{jj'} \delta_{\lambda\lambda'} \\ \langle J'_A \Omega'_A | J_A^2 | J_A \Omega_A \rangle &= \hbar^2 J_A(J_A+1) \delta_{J_A J'_A} \delta_{\Omega_A \Omega'_A} \end{aligned}$$

The coupling terms between angular momenta are solved using the *ladder operators*  $\hat{\mathcal{J}}_+$  and  $\hat{\mathcal{J}}_-$  [19] —for a generic angular momentum,  $\hat{\mathcal{J}}_+ = \hat{\mathcal{J}}_x + i\hat{\mathcal{J}}_y$  and  $\hat{\mathcal{J}}_- = \hat{\mathcal{J}}_x - i\hat{\mathcal{J}}_y$ .

$$\begin{aligned} \langle J\Omega' j' J'_A \Omega'_A p | \ell^2 | J\Omega j J_A \Omega_{AP} \rangle &= \delta_{jj'} \delta_{J_A J'_A} \{ \delta_{\Omega\Omega'} \delta_{\Omega_A \Omega'_A} \hbar^2 \times & (1.31) \\ & [J(J+1) + j(j+1) + J_A(J_A+1) - 2\Omega^2 - 2\Omega_A^2 + 2\Omega\Omega_A] \\ & - d_{\Omega\Omega' \Omega_A \Omega'_A} \langle J\Omega j J_A \Omega_{AP} | \ell_{coup}^2 | J\Omega j J_A \Omega_{AP} \rangle \} \\ \ell_{coup}^2 &\equiv J_+ j_- + J_- j_+ + J_+ J_{A-} + J_- J_{A+} - j_+ J_{A-} - j_- J_{A+} \end{aligned}$$

The coefficient  $d_{\Omega\Omega' \Omega_A \Omega'_A}$  can adopt the value  $\sqrt{2}$  if either  $\Omega, \Omega', \Omega_A$  or  $\Omega'_A$  are zero, but otherwise  $d_{\Omega\Omega' \Omega_A \Omega'_A} = 1$ .

For the sake of simplicity, the analytical expression of the ladder operators is not explicitly written, yet their evaluation is trivial if their general definition is considered.

$$\hat{\mathcal{J}}_{\pm} |J\Omega\rangle = \hbar \sqrt{J(J+1) - \Omega(\Omega \pm 1)} |J\Omega \pm 1\rangle \quad (1.32)$$

## Potential Elements

The potential matrix elements are obtained, in analogy with the kinetic elements, by representing the electronic potential energy operator  $\widehat{V}$  in the already defined basis functions of the system  $|J\Omega j J_A \Omega_A p\rangle$ . Although the final evaluation in the chosen basis is not very different from the previous cases, the electronic potential is considerably more complex to obtain. The selection of a specific methodology to calculate the potential is often conditioned to the way the main problem is addressed. Hence, to let the reader have a deeper understanding of the main topic of this study, the explicit form of these matrix elements will be shown later in section 2.2.5.

## 1.3 Reaction Dynamics: Quantum Models

From a microscopic point of view, any chemical reaction can be understood as a collisional process in which there is a change in the arrangement of the atoms of the system (*i.e.* there is a change in the chemical species). For a given asymptotic arrangement, the internal state of all species is completely determined by the collection of quantum numbers that define the wavefunction. This is what is known as a *reaction channel* [17]. In the present system of study, the channels are defined as follows within a given arrangement—in the asymptotic electronic state labelled as  $i_e$  and parity  $p$ .

$$\alpha \equiv \{i_e, j, v, J_A, \Omega_A\} \quad \text{with constant the values of } \{E, J, p\} \quad (1.33)$$

Note that this nomenclature excludes the total energy  $E$ , total angular momentum  $J$  and parity  $p$  from the channel labels  $\alpha$ . They are expected to be conserved for all involved channels as they correspond to definite eigenvalues of the *complete set of commuting operators* of the system [21]—*i.e.* the Hamiltonian  $\widehat{H}$ , the total angular momentum  $\widehat{J}^2$  and the inversion operator  $\mathcal{E}^*$ .

For the reactant arrangement, there is one additional feature which strongly affects the nature of the channels. It is a consequence of the nuclear spin configuration of the  $\text{H}_2$  fragment (either *ortho* or *para*). In this study, the hyperfine interaction terms are not included because of their small magnitude. Nonetheless, as the nuclear spin function is exactly separable for a diatomic molecule (two nuclei system), the diatomic permutation symmetry is indeed rigorously covered. It is introduced *a posteriori* by taking its effects on the diatomic rotational quantum number  $j$ —the configuration p- $\text{H}_2$

only allows even values of  $j$ , while the o-H<sub>2</sub> only allows odd values. For this reason, an artificial quantum number  $p_d$  is introduced corresponding to this *diatomic parity* — ' $p_d = \text{even}$ ' means even  $j$  values, yet ' $p_d = \text{odd}$ ' allows odd  $j$  values [24].

Although many different channels may exist for a certain arrangement, the system can only access with a certain probability some of them for a given total energy  $E$  — called *open channels* as opposed to the inaccessible *closed channels* [28].

The probability of starting from a specific reactant channel  $\alpha$  and ending in another product channel  $\alpha'$  is represented by the so-called *state-to-state reaction probability*  $P_{\alpha\Omega \alpha'\Omega'}^{Jp}(E)$  [29]. The estimation of this probability is the central motivation of the theoretical simulations and approximations of this study, as it is carefully explored in the next sections.

The *state-to-state reaction probabilities*  $P_{\alpha\Omega \alpha'\Omega'}^{Jp}(E)$  can be used to obtain the useful *state-to-state cross-section*  $\sigma_{\alpha\alpha'}(E)$  from a partial wave summation over the total angular momentum  $J$ .

$$\sigma_{\alpha\alpha'}(E) = \frac{\pi}{(2j+1)(2J_A+1)k_\alpha^2(E)} \sum_{J_p} \sum_{\Omega\Omega'} (2J+1) P_{\alpha\Omega \alpha'\Omega'}^{Jp}(E) \quad (1.34)$$

with

$$k_\alpha(E) = \frac{\sqrt{2\mu(E - E_\alpha)}}{\hbar} \quad (1.35)$$

Although the microscopic behaviour of the reaction is already characterized by the *state-to-state cross-section*  $\sigma_{\alpha\alpha'}(E)$ , it is often preferred to handle macroscopic magnitudes such as *thermal rate constants*  $K(T)$  [5, 7]— yet cross-sections can also be experimentally measured if desired [6]. Consequently, it is needed to build the *state-to-state rate constants*  $K_{\alpha\alpha'}(T)$  by performing Boltzmann averages over the total energy  $E$ , and finally estimate the macroscopic mean *thermal rate constant*  $K(T)$  assisted by an average arising from statistical mechanics [15].

$$K_{\alpha\alpha'}(T) = \sqrt{\frac{8}{\pi\mu(k_B T)^3}} \int dE E \sigma_{\alpha\alpha'}(E) e^{-E/k_B T} \quad (1.36)$$

$$K(T) = \sum_{v j i_e} w_\alpha(T) \sum_{\alpha'} K_{\alpha\alpha'}(T)$$

$$w_\alpha(T) = \frac{(2I_{BC}+1)(2j+1)(2J_A+1)e^{-E_\alpha/k_B T}}{\sum_{\alpha''} (2I_{BC}+1)(2j+1)(2J_A+1)e^{-E_{\alpha''}/k_B T}}$$

### 1.3.1 Resonance-driven reactions

As a matter of fact, there are two possible ways for a reaction to take place. These are either going from a specific channel to another *open channel* — a direct, classical process —, or ending in an initially *closed channel* which has been coupled to other accessible channels — indirect, quantum process. The latter mechanism is known as a *resonance* [30–32], and occurs when the system gets trapped in potential wells forming a *collision complex* — long-lived *collision complexes* imply a loss of information of the initial state. Depending on the nature of the coupled channels, one can distinguish between *Feshbach resonances* — coupling different channels (electronic, vibrational, rotational ...) —, or *orbital resonances* — coupling unbound continuum states with bound vibrational states within the same channel (*quasi-bound states* supported by a centrifugal barrier).

Following with what is described in the next section, the *reaction probability*  $P(E)$  can be equivalently expressed in terms of the *scattering matrix*  $S(E)$ . As it will be shown in section 2.1.4, the origin of this magnitude lies in the heart of the quantum collisional process. Therefore, it is not surprising that the *scattering matrix* can be conceptually decomposed into the two possible reaction mechanisms — according to *W. H. Miller* [30].

$$S(E) = S_{bg} \left( 1 - \frac{iA}{E - E_r + i\Gamma} \right) \quad (1.37)$$

The *background* direct mechanism contribution  $S_{bg}$  arises from the interactions of the open channels. However, the second *resonance* indirect term depends on the coupling between open and closed channels ( $A$ ). For a *resonance* to occur, a specific energy  $E_r$  is required, with a specific lifetime related to its width  $\Gamma$ . What is clear is that the *resonances* are the poles of the *scattering matrix* in the complex plane.

In systems where there are many different channels close to each other in energy, the importance of the *resonances* becomes critical. In the system of this study, there are multiple channels in an intermediate region where a deep well in the Potential Energy Surfaces occurs — the system gets "trapped" in the well for a while [7, 15].

For this reason, this particular insertion reaction is said to be a *resonance driven reaction*. Additionally, under these conditions the statistical model is expected to give accurate descriptions of the system, since all coupled channels become almost equally probable — the system loses its "memory", and gets an unbiased capture in a certain channel once it leaves the well.

### 1.3.2 Statistical method: Capture model

In view of the previous section, the only difficulty is how to estimate the *state-to-state reaction probabilities*  $P_{\alpha\Omega, \alpha'\Omega'}^{Jp}(E)$  — or equivalently, the so-called *state-to-state scattering matrix*  $S_{\alpha\Omega, \alpha'\Omega'}^{Jp}$ , related as  $P_{\alpha\Omega, \alpha'\Omega'}^{Jp}(E) = |S_{\alpha\Omega, \alpha'\Omega'}^{Jp}|^2$  [30]. This quantity can be calculated in many different ways, but the chosen *statistical approach* is characterized by using *capture probabilities* for each channel  $C_{\alpha\Omega}^{Jp}$ .

$$P_{\alpha\Omega, \alpha'\Omega'}^{Jp}(E) = C_{\alpha\Omega}^{Jp} B_{\alpha'\Omega'}^{Jp}(E) \quad B_{\alpha'\Omega'}^{Jp}(E) = \frac{C_{\alpha'\Omega'}^{Jp}}{\sum_{\alpha''\Omega''} C_{\alpha''\Omega''}^{Jp}} \quad (1.38)$$

where  $B_{\alpha'\Omega'}^{Jp}(E)$  is the *branching ratio* accounting on all the accessible channels from all the possible arrangements.

The calculation of the *capture probabilities* is performed in this study in two different approaches: *quantum statistical* and *adiabatic statistical* models.

The *adiabatic statistical* method [28, 33, 34] simply imposes a classical approximation — either completely opened or closed channels, no intermediate probabilities. For a specific *adiabatic* eigenvalue of the total potential matrix, if the highest energy barrier is denoted as  $E_b$ , the capture is given by equation (1.39).

$$C_{\alpha\Omega}^{Jp} = \begin{cases} 1 & \Leftrightarrow E \geq E_b \\ 0 & \Leftrightarrow E < E_b \end{cases} \quad (1.39)$$

On the other hand, the *quantum statistical* approach [26, 27, 29, 35] assigns a certain probability to each channel (between 0 and 1), which is found by solving a set of inelastic *close-coupled* equations for each arrangement, as described in section 2.2.

# Chapter 2

## Methodology

The main focus of this study is to stress the importance of resonances in the reactivity of simple systems such as in the model reaction  $\text{N}^+ + \text{H}_2 \longrightarrow \text{NH}^+ + \text{H}$ , as well as its implications for the system to behave in a statistical way. For this reason, the first part of this study is dedicated to the proper illustration of the concept of resonance for a simple one-dimensional case (section 2.1), along with the description of the numerical methods applied in the actual implementation of the *time-independent* Schrödinger equation. Then, the system of interest is fully explored and discussed by a generalization of the previously seen concepts, with a program developed for solving the so-called *close-coupling* equations and get a quantum-statistical model for the dynamics. The validation of this methodology is presented as well, by comparing the obtained results with those given by a complete numerically-exact *time-dependent* method, analysing both their strengths and weaknesses — the latter actually treats both the direct and indirect (resonance mediated) reaction mechanisms.

### 2.1 Numerical methods and Resonances

#### 2.1.1 One-dimensional model potential

As it was stated before in section 1.3.1, resonances play a fundamental role in the reactivity of some systems which behave statistically due to the coupling between open channels and closed channels [30]. Although they exhibit their greatest power in multi-dimensional systems, such as the one of interest in this study  $\{R, r, \gamma\}$ , the visualization of their basic nature is rather achieved for simple one-dimensional cases.

Taking this argument as a foundation, in this section it is considered as a

model system a simple *Eckart potential* [36], the "smooth" equivalent to a *step potential* ( $V_0$ ) at  $R_0$ , with a *barrier* ( $V_b$ ) of width  $L$  — see Figure 2.1.

$$V = V_0 \frac{-\xi}{1-\xi} + V_b \frac{-\xi}{(1-\xi)^2} \quad \xi \equiv -\exp\left(2\pi \frac{R-R_0}{L}\right) \quad (2.1)$$

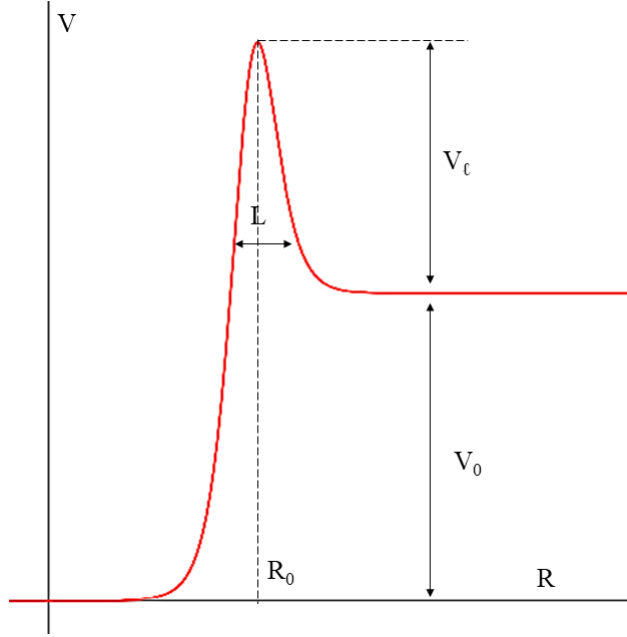


Figure 2.1: Generic Eckart potential

Note that the exact barrierless *step potential* is just the limit case of the *Eckart potential* when  $L \rightarrow 0$  and  $V_b \rightarrow 0$  — the limit of interest in this simplification.

It is worth to mention that, in analogy to the more complex system of study  $\text{NH}_2^+$ , there is a certain *rotational barrier*  $\frac{\hbar^2 \ell(\ell+1)}{2\mu R^2}$  arising from the angular momentum  $\ell$ . This introduces an additional distortion on the potential, so that the *effective potential*  $\mathcal{V}$  must account on it.

$$\mathcal{V} = V + \frac{\hbar^2 \ell(\ell+1)}{2\mu R^2} \quad (2.2)$$

As we are interested in obtaining the eigenstates of the system ( $\Phi$ ), the resolution of the *time-independent* Schrödinger equation is required, as usual.

$$\Phi'' = \frac{2\mu}{\hbar^2} (\mathcal{V} - E) \Phi \quad (2.3)$$

for which it is expected to find both bound  $|\Phi_i\rangle$  and continuum solutions  $|\Phi_E\rangle$ , so the general closure relation holds [21].

$$\sum_i |\Phi_i\rangle \langle \Phi_i| + \int dE |\Phi_E\rangle \langle \Phi_E| = 1 \quad (2.4)$$

### 2.1.2 Discrete representations

Before any numerical method is applied to solve this equation, it is needed to take a discrete space-representation of the functions by introducing a grid for the coordinate  $R$  with a spacing of  $\Delta$  [17].

$$|R_k\rangle = \begin{cases} 0 \Leftrightarrow R \notin (R_k - \frac{\Delta}{2}, R_k + \frac{\Delta}{2}) \\ \sqrt{1/\Delta} \Leftrightarrow R \in (R_k - \frac{\Delta}{2}, R_k + \frac{\Delta}{2}) \end{cases} \quad (2.5)$$

$$\lim_{\Delta \rightarrow \infty} \langle R_j | R_k \rangle = \delta(R_j - R_k)$$

The wavefunction is expanded in the new discrete basis, as well as the potential—which is assumed to be quasi-constant between two adjacent grid points.

$$\Phi = \sum_k \Phi_k |R_k\rangle \quad (2.6)$$

$$\langle R_j | \mathcal{V} | R_k \rangle = \delta_{jk} \mathcal{V}(R_k) \equiv \mathcal{V}_k$$

By working in the new discrete representation, it is possible to introduce numerical approximations which can be implemented in actual computer programs. This way, it is possible to find numerical solutions to the discretized *time-independent* Schrödinger equation.

$$\Phi_k'' = \frac{2\mu}{\hbar^2} (\mathcal{V}_k - E) \Phi_k \quad (2.7)$$

The numerical techniques used in this study (*i.e.* Numerov and Givens) are both based on Taylor expansions of the coefficients of the wavefunction in the discrete basis, which are assumed to be continuous in all intervals—as well as their derivatives, forming the postulates of the *Finite Difference method* [37].

$$\Phi_{k\pm 1} = \Phi_k \pm \Delta \Phi_k' + \frac{\Delta^2}{2!} \Phi_k'' \pm \frac{\Delta^3}{3!} \Phi_k''' + \frac{\Delta^4}{4!} \Phi_k^{iv} + \dots \quad (2.8)$$

The actual factorization and manipulation of these equations are the starting points for the approximations to be done in the different numerical methods of this study. For this one-dimensional case, the Numerov method will be applied.

### 2.1.3 Numerov method

Within the Numerov method [17, 37], the Taylor expansion of the wavefunction is truncated up to sixth order  $\mathcal{O}(\Delta^6)$ , and some summations are performed taking the Taylor expansion of the wavefunction and its derivatives.

$$\begin{cases} \Phi_{k+1} + \Phi_{k-1} \approx 2\Phi_k + \Delta^2\Phi_k'' + \frac{\Delta^4}{12}\Phi_k^{iv} \\ \frac{-\Delta^2}{12}(\Phi_{k+1}'' + \Phi_{k-1}'') \approx -\frac{\Delta^2}{6}\Phi_k'' - \frac{\Delta^4}{12}\Phi_k^{iv} \end{cases} \Rightarrow \quad (2.9)$$

$$(\Phi_{k+1} + \Phi_{k-1}) - \frac{\Delta^2}{12}(\Phi_{k+1}'' + \Phi_{k-1}'') \approx 2\Phi_k + \frac{5\Delta^2}{6}\Phi_k'' \Rightarrow$$

Substituting the second-derivatives by their definition in the discretized *time-independent* Schrödinger equation, the final expression becomes as seen in equation (2.10).

$$\boxed{\alpha_{k-1}\Phi_{k-1} + \beta_k\Phi_k + \gamma_{k+1}\Phi_{k+1} \approx 0} \quad (2.10)$$

$$\alpha_{k-1} = 1 - \frac{\Delta^2}{12}\lambda_{k-1} \quad \beta_k = -2 - \frac{10\Delta^2}{12}\lambda_k \quad \gamma_{k+1} = 1 - \frac{\Delta^2}{12}\lambda_{k+1}$$

$$\lambda_k = \frac{2\mu}{\hbar^2}(V_k - E)$$

With this key equation of the method, a propagator  $\mathcal{R}_k$  is defined to interrelate the wavefunction at two adjacent grid-points.

$$\Phi_k = \mathcal{R}_k\Phi_{k+1} \quad \mathcal{R}_k = -[\alpha_{k-1}\mathcal{R}_{k-1} + \beta_k]^{-1}\gamma_{k+1} \quad (2.11)$$

This way, once the suitable boundary conditions are imposed on the asymptotic regions ( $R \rightarrow 0$  and  $R \rightarrow \infty$ ), the wavefunction is completely known at all grid points — two boundary conditions are required to fully characterize the solutions of the second-order differential equation. The propagation is developed from the left asymptote ( $R \rightarrow 0$ ), and when the last point is reached ( $R \rightarrow \infty$ ), the right boundary condition is imposed too.

Of course, the algorithm presented above corresponds to the one-dimensional version of *Numerov's method*. In practice, when multiple channels are involved, the equations are recast into a matrix form —as shown in section 2.2.

### 2.1.4 Boundary conditions

The proper definition of the boundary conditions strongly depends on the potential considered, which determines the actual form of the wavefunction of the system. As usually happens for most typical molecular potentials, in the asymptotic regions of the reactants and products arrangements, the potential becomes flat and the wavefunction behaves asymptotically as the ordinary solutions of a *step potential*.

In the case of a one-dimensional potential with an isolated *centrifugal barrier*, the radial Schrödinger equation adopts the form seen in equation (2.12).

$$\left[ \frac{-\hbar^2}{2\mu} \frac{d^2}{dR^2} + \frac{\hbar^2 \ell(\ell+1)}{2\mu R^2} - (E - V) \right] \Phi_E^\ell = 0 \quad (E - V) = \frac{\hbar^2 k^2}{2\mu} \quad (2.12)$$

After a small manipulation of the previous equation, when  $V = 0$  (*i.e.* long distances for which  $V \rightarrow 0$  faster than  $R^{-2}$ ), one can finally conclude that its solutions are the well-known *spherical Bessel functions of first* ( $j_\ell$ ) and *second* kind ( $y_\ell$ ) — called *regular* and *irregular* solutions, respectively [38].

$$\Phi_E^\ell = \begin{cases} AkR j_\ell(kR) \\ AkR y_\ell(kR) \end{cases} \underset{R \rightarrow \infty}{=} \begin{cases} A \sin\left(kR - \ell\frac{\pi}{2}\right) \\ -A \cos\left(kR - \ell\frac{\pi}{2}\right) \end{cases} \quad (2.13)$$

These are real stationary solutions, but it is also possible to get incoming and outgoing complex solutions by taking linear combinations of them (*i.e.* *Bessel functions of third order*  $h_\ell^{(1)} = j_\ell + iy_\ell$  and  $h_\ell^{(2)} = j_\ell - iy_\ell$ ) [38].

$$\Phi_E^{\ell\pm} = \begin{cases} A^\pm kR h_\ell^{(1)}(kR) \\ A^\pm kR h_\ell^{(2)}(kR) \end{cases} \underset{R \rightarrow \infty}{=} \begin{cases} iA^\pm e^{-i(kR - \ell\frac{\pi}{2})} \\ -iA^\pm e^{i(kR - \ell\frac{\pi}{2})} \end{cases} \quad (2.14)$$

These last asymptotic solutions are by definition eigenfunctions of the linear momentum operator — as well as eigenfunctions of the Hamiltonian —, as seen in equation (2.15).

$$\hat{p} = -i\hbar \frac{\partial}{\partial R} \quad \hat{p} \Phi_E^{\ell\pm}(R) = \pm\hbar k \Phi_E^{\ell\pm}(R) \quad (2.15)$$

The norm factor  $A$  is trivially obtained by imposing the energy normalization condition.

$$\langle \Phi_E^{\ell\pm} | \Phi_{E'}^{\ell\pm} \rangle = \delta(E - E') \quad A^\pm = \sqrt{\frac{\mu}{2\pi k \hbar^2}} \quad (2.16)$$

If we work with the real stationary solutions instead of the complex incoming and outgoing waves, the norm factor is multiplied by two ( $A = 2A^\pm$ ), as they involve the combination of two exponential functions.

Although this example is just constrained to a one-dimensional potential for the sake of simplicity, the exact same boundary conditions can be generalized to the multi-dimensional case for more complex systems as the one chosen for this study,  $\text{NH}_2^+$ .

Recalling the case of a one-dimensional *Eckart potential* [36], there are two boundary conditions to consider. Suppose a hypothetical particle approaching the barrier from the right-hand side.

The left asymptote  $\Phi_E^{\ell(I)}(R \rightarrow 0)$  imposes the condition of an *outgoing wave*, leaving the barrier in the right. Conversely, in the right asymptote  $\Phi_E^{\ell(II)}(R \rightarrow \infty)$ , the wavefunction is a superposition of transmitted and reflected functions.

$$\Phi_E^{\ell(I)} = N_I e^{-ik_I R} \quad \Phi_E^{\ell(II)} = N_{II} [e^{-ik_{II} R} - S e^{ik_{II} R}] \quad (2.17)$$

Where  $S$  is the *scattering matrix*. As stated before, it is a fundamental magnitude because it keeps the most relevant information of the whole dynamical process, and is often needed for the obtention of other important magnitudes like the *reaction cross-section* — as in the  $\text{NH}_2^+$  reaction.

There are alternative formulations of the *scattering matrix* [17], which arise from the general expression of the wavefunction — matching equations (2.17).

$$\begin{aligned} \Phi_E^{\ell}(R) &= N [\sin(kR) + K \cos(kR)] = N' \sin(kR + \delta) \\ S &= e^{i2\delta} = [1 - iK]^{-1} [1 + iK] \end{aligned} \quad (2.18)$$

This way, it is clear that the *scattering matrix* conceptually emerges from the energy-dependent phase  $\delta$ , or equivalently the so-called *reaction matrix*  $K = \tan(\delta)$ . Despite this simple origin, they give crucial information about the effect of the potential on the asymptotic behaviour of the dissociative eigenstates (*i.e.* reaction channels).

### 2.1.5 Numerical Propagation

The numerical method begins with the forward propagation of the wavefunction in the discrete grid defined in 2.1.2. Taking the asymptotic right boundary condition [38], if the effective potential at  $R \rightarrow 0$  is sufficiently higher than the energy, and if the grid step is small enough, the propagator can be easily initialized using that  $\Phi_k = \mathcal{R}_k \Phi_{k+1}$ .

$$\mathcal{R}_1 = 0 \quad (\mathcal{V} \gg E) \quad (2.19)$$

Then, applying the *Numerov method* [37], the forward propagation is achieved using equations (2.10) and (2.11) at each point.

$$\mathcal{R}_k = -[\alpha_{k-1} \mathcal{R}_{k-1} + \beta_k]^{-1} \gamma_{k+1}$$

Once the forward propagation has reached the last grid point, it is time to perform a backward propagation too, as part of Numerov's method. At the right asymptote, the wavefunction is fully characterized, so that the *scattering matrix* is trivially found from  $\Phi_{n-1} = \mathcal{R}_{n-1} \Phi_n$ .

$$S = \frac{\mathcal{R}_{n-1} e^{-ik_{II} R_n} - e^{-ik_{II} R_{n-1}}}{\mathcal{R}_{n-1} e^{ik_{II} R_n} - e^{ik_{II} R_{n-1}}} \quad (2.20)$$

Note that, for a certain potential and a *rotational barrier* arising from a fixed angular momentum  $\ell$ , the *scattering matrix* is a unique function which only depends on the energy.

Since the propagator is already known at all grid points, the final recovery of the wavefunction and the *scattering matrix* is possible by the inverse propagation mechanism —  $\Phi_k = \mathcal{R}_k \Phi_{k+1}$ .

With this simple one-dimensional example in section 2.1, all the details concerning Numerov's method are already shown. They are exactly the same for the general multi-dimensional problems — recast in a matrix formulation though.

## 2.2 Time-independent approach

### 2.2.1 Multi-dimensional potential and grids

The main focus of this study is devoted to the theoretical modellization of the system  $\text{NH}_2^+$ , being its asymptotes the reactants ( $\text{N}^+ + \text{H}_2$ ) and products ( $\text{NH}^+ + \text{H}$ ) arrangements — which are calculated separately, but later combined in the statistical method. Although it consists in a multi-dimensional potential problem — *i.e.* three internal coordinates  $\{R, r, \gamma\}$  —, the formal treatment is analogous to what has been described in section 2.1. Note that all the explained methodology was implemented into a computer program called *aZticc* [39] which is briefly described in section 2.2.5.

Let us recall the chosen expansion of the total nuclear wavefunction of the system

$$\Psi_E^J(R, r, \gamma, \phi, \theta, \chi) = \sum_{\alpha} \frac{\Phi_{\alpha}(R)}{R} \frac{\varphi_{jv}(r)}{r} \mathcal{W}_{jJ_A\Omega_A}^{J\Omega}(\gamma, \phi, \theta, \chi) \quad (2.21)$$

The angular basis  $\mathcal{W}_{jJ_A\Omega_A}^{J\Omega}$  is exactly known from the expression of the *spherical harmonics* and *Wigner rotation matrices* [22], hence there is only left to numerically compute the radial functions  $\Phi_{\alpha}(R)$  and  $\varphi_{jv}(r)$ . In any case, the actual application of the wavefunction in computer codes encourages us to discretize the functions by introducing discrete grids on the selected coordinates of the system  $\{r, R, \gamma\}$ .

The *ab initio* potentials are also subject to the discretization of the coordinates, but they are rather saved in a *Discrete Variable Representation* (DVR) [37]. It is just the selection of optimized grid points which correspond to the roots of selected expansion functions in which the potential is integrated for storage — in this case, Gauss-Legendre integration with associated Legendre polynomials as expansion functions.

It is time to explain how the numerical methods of this study are implemented. Let us illustrate the procedure with a general discretized function  $|\psi\rangle = \sum_k \psi_k |k\rangle$ , yet the discussion is valid both for  $\Phi_{\alpha}(R)$  and  $\varphi_{jv}(r)$ . By definition of the *finite difference method* [37], the grid elements are separated by a step  $\Delta$ , in which both the wavefunction (*i.e.* its coefficients  $\psi_k$ ) and its derivatives are assumed to be continuous. Then, the Taylor expansion of the coefficients is performed in the finite grid.

This expansion is combined with the actual numerical problem that must be solved, the discretized expression of the *time-independent* Schrödinger equation.

$$\psi_k'' = \frac{2\mu}{\hbar^2}(\mathcal{V}_k - E)\psi_k \quad (2.22)$$

The factorization and manipulation of these two equations are the starting points for the approximations to be done in the different numerical methods of this study.

### 2.2.2 Given's method

The diatomic function  $\varphi_{jv}(r)$  is found by application of the *Given's method* [17,37] to solve the discretized *time-independent* Schrödinger equation of the diatomic fragment —  $\varphi_k'' = \frac{2\mu}{\hbar^2}(V_k - E)\varphi_k$ . The Taylor expansion is truncated at fourth order  $\mathcal{O}(\Delta^4)$ , and the summation  $\varphi_{k+1} + \varphi_{k-1}$  is performed to eliminate the odd powers of  $\Delta$ .

$$\varphi_{k+1} + \varphi_{k-1} \approx \left(2 + \frac{2\mu}{\hbar^2}(V_k - E)\right) \varphi_k \quad (2.23)$$

If we define  $H_k \equiv -2 - \frac{2\mu\Delta^2}{\hbar^2}V_k$ , the matrix form of the equation becomes.

$$\begin{pmatrix} H_1 & 1 & 0 & \cdots & 0 \\ 1 & H_2 & 1 & \cdots & 0 \\ 0 & 1 & H_3 & \cdots & 0 \\ \vdots & \vdots & \vdots & \ddots & \vdots \\ 0 & 0 & 0 & \cdots & H_n \end{pmatrix} \begin{pmatrix} \varphi_1 \\ \varphi_2 \\ \varphi_3 \\ \vdots \\ \varphi_n \end{pmatrix} \approx \begin{pmatrix} 1 & 0 & 0 & \cdots & 0 \\ 0 & 1 & 0 & \cdots & 0 \\ 0 & 0 & 1 & \cdots & 0 \\ \vdots & \vdots & \vdots & \ddots & \vdots \\ 0 & 0 & 0 & \cdots & 1 \end{pmatrix} \lambda \begin{pmatrix} \varphi_1 \\ \varphi_2 \\ \varphi_3 \\ \vdots \\ \varphi_n \end{pmatrix} \quad (2.24)$$

$$\lambda = \frac{-2\mu\Delta^2}{\hbar^2}E$$

where the Hamiltonian matrix has a tridiagonal form trivially diagonalized by standard subroutines — *e.g.* the TQLI algorithm [37].

### 2.2.3 Numerov-Fox-Goodwin method

The radial coefficients  $\Phi_\alpha(R)$ , which depend on the main reaction coordinate  $R$ , are found by application of the multi-dimensional version of *Numerov method (Numerov-Fox-Goodwin)* [40,41] to solve the discretized radial *time-independent* Schrödinger equation for the whole system —  $\bar{\Phi}_k'' = \frac{2\mu}{\hbar^2}(\bar{\mathcal{V}}_k - E\bar{\mathbb{I}})\bar{\Phi}_k$ .

Note that the parameters  $\bar{\alpha}_{k-1}$ ,  $\bar{\beta}_k$  and  $\bar{\gamma}_{k+1}$  are now matrices, and the wavefunction  $\bar{\Phi}_k$  is actually a vector, accounting on all the possible channels within each arrangement.

$$\boxed{\bar{\alpha}_{k-1}\bar{\Phi}_{k-1} + \bar{\beta}_k\bar{\Phi}_k + \bar{\gamma}_{k+1}\bar{\Phi}_{k+1} \approx 0} \quad (2.25)$$

$$\begin{aligned} \bar{\alpha}_{k-1} &= 1 - \frac{\Delta^2}{12}\bar{\lambda}_{k-1} & \bar{\beta}_k &= -2 - \frac{10\Delta^2}{12}\bar{\lambda}_k & \bar{\gamma}_{k+1} &= 1 - \frac{\Delta^2}{12}\bar{\lambda}_{k+1} \\ \bar{\lambda}_k &= \frac{2\mu}{\hbar^2}(\bar{V}_k - E\bar{\mathbb{I}}) \end{aligned}$$

The propagator matrix  $\bar{\mathcal{R}}_k$  is defined, so that  $\bar{\Phi}_k = \bar{\mathcal{R}}_k\bar{\Phi}_{k+1}$ , and again  $\bar{\mathcal{R}}_k = -[\bar{\alpha}_{k-1}\bar{\mathcal{R}}_{k-1} + \bar{\beta}_k]^{-1}\bar{\gamma}_{k+1}$ . This way, once the suitable boundary conditions are imposed on the asymptotic regions ( $R \rightarrow \infty$ ), the wavefunction is completely known at all grid points.

As in the one-dimensional case, the propagation of the wavefunction is performed from both asymptotes by imposing the suitable boundary conditions, which allows the numerical resolution of the problem.

## 2.2.4 Boundary conditions

The calculations of the *reactant* and *product* arrangements are performed separately, under the assumptions of a capture model once the system escapes from the deep potential well. As a consequence, the boundary conditions to impose for each asymptotic channel are quite similar to those already described in the one-dimensional case — combinations of third order *Bessel functions*  $h_\ell^{(1)}$  and  $h_\ell^{(2)}$  [38].

$$\Phi_E^\ell = \begin{cases} AkR h_\ell^{(1)}(kR) \\ AkR h_\ell^{(2)}(kR) \end{cases} \quad R \rightarrow \infty \quad = \quad \begin{cases} iA e^{-i(kR - \ell\frac{\pi}{2})} \\ -iA e^{i(kR - \ell\frac{\pi}{2})} \end{cases} \quad (2.26)$$

In the left (reactant) asymptote, for the adiabatic diagonalized potential  $V_\alpha^d$ , an *outgoing solution* is imposed for open-channels, but it vanishes for closed channels, in agreement to the postulates of the capture model — remember that the capture probability is  $|S_\alpha(E)|^2$  and  $k_\alpha = \sqrt{\frac{2\mu(E - V_\alpha^d)}{\hbar^2}}$ .

$${}^1\Phi_\alpha(R < R_1) = \begin{cases} 0 & \Leftrightarrow E < V_\alpha^d \\ -i\sqrt{\frac{2\mu}{\pi\hbar^2 k_\alpha}} S_\alpha(E) e^{-ik_\alpha R} & \Leftrightarrow E \geq V_\alpha^d \end{cases} \quad (2.27)$$

In the right (product) asymptote, the usual superposition of incoming and outgoing solutions is imposed as shown below.

$$\Phi_\alpha(R > R_N) = \begin{cases} e^{-i|k_\alpha|R} & \Leftrightarrow E < V_{\alpha,\alpha} \\ i\sqrt{\frac{2\mu}{\pi\hbar^2 k_\alpha}} S_\alpha(E) [e^{-ik_\alpha R - \ell\frac{\pi}{2}} - S_{\alpha\beta} e^{ik_\alpha R - \ell\frac{\pi}{2}}] & \Leftrightarrow E \geq V_{\alpha,\alpha} \end{cases} \quad (2.28)$$

As a matter of fact, the spherical *Bessel functions* are built for a well-defined value of the angular momentum quantum number  $\ell$ , which is only fulfilled for a *space-fixed* frame. Unfortunately, all the formal treatment of the problem has been developed in a *body-fixed* coordinate system to facilitate the computation of the basis functions and matrix elements. For this reason, the *aZticc* program [39] roughly estimates an average value of  $\ell$  by diagonalizing its corresponding Coriolis matrix (of eigenvalues  $\ell_d$ ) and rounding to the closest integer value.

$$\ell_d \approx \ell(\ell + 1) \Rightarrow \ell \approx \frac{1}{2} \left[ -1 + \sqrt{1 + 4\ell_d} \right] \quad (2.29)$$

The quality of this rough approximation is ensured by checking the predicted  $\ell$  value from the energy difference at the right asymptote — only the Coriolis terms may present significant discrepancies.

$$\Delta E \approx \frac{\hbar^2 \ell(\ell + 1)}{2\mu} \left[ \frac{1}{R_{N-1}} - \frac{1}{R_N} \right] \quad (2.30)$$

### 2.2.5 The 'aZticc' program

The main theoretical concepts and numerical methodology of this study has been implemented in the FORTRAN [42] code *aZticc* — *Adiabatic Complex Time-Independent Close-Coupling* solver —, specially developed by *O. Roncero* [39] for this work. Its final objective is to estimate the capture probabilities by solving a set of inelastic close-coupled equations for each arrangement separately to be further used in statistical calculations.

Its core approximations are, apart from the capture model and both *adiabatic* and *quantum* statistical approaches, the Numerov propagation [40] with an *adiabatic-by-sectors* representation [43–45].

The power of this *adiabatic-by-sectors* technique for the Numerov propagation lies in the possibility to reduce the number of channels without drastically

affecting the quality of the approximation. Unlike the *diabatic* channels, the *adiabatic* channels are ordered by their energy  $E_\rho(R)$ , so it is possible to only keep those channels with an energy below the imposed truncation energy  $E_{cut}$  ( $E_\rho(R) < E_{cut}$ ).

A complete description of this methodology will not be provided in this master thesis, but it can be found in the upcoming reference article *Gómez-Carrasco et al.* [39] by this research group.

### Potential Energy selection

In this section, a more detailed explanation about the potential elements is given. There are two sets of potential energy surfaces (PES) that have been used in this study, each of them for different purposes.

The first set, corresponding to the ones obtained by *Nyman et al.* [12] is just a collection of two *adiabatic* ground-state PES — one optimal for each arrangement. Each of them are complete surfaces from the reactant to the product asymptotic arrangements, without skipping the intermediate regions, but they lack any spin-orbit considerations.

This considerable simplification makes this set of PES only suitable for minor qualitative calculations such as the study of the effect of the different basis parameters, or the comparison with time-dependent approaches — validation calculations and mostly didactic purposes.

The second set of PES has been developed by the present research group, which not only introduces long-range corrections to the numerous *adiabatic* spin-orbit states — later diabitized as explained below —, but also accounts on the actual spin-orbit splittings for each of them. This increases the number of total electronic states to 9 in the reactant arrangement, and 11 in the product arrangement. The complexity of this set of PES makes it the ultimate choice for accurate quantitative results of cross-sections and rate constants — the one used in the upcoming article *Gómez-Carrasco et al.* [39]. In view of this, only this last PES set will be described in the present section.

It is important to stress that, despite that the complete spin-orbit states are considered, the PES developed by the present research group are limited to only the reactant and product arrangement regions. The *statistical approximation* makes possible to treat each arrangement separately for simplicity, which allows a more detailed description of those regions. After all, for the *statistical model*, it is all which is required, and for this reason it can be said that it is a more detailed PES — without forgetting the particularities of both PES sets.

As long as the optimal definition of the Jacobi coordinates differ for the *reactant* and *product arrangements*, two distinct PES were developed (one for each arrangement) with slightly different features. Anyway, they share common basic steps, so that their discrepancies are indicated when needed. In all cases, the final PES have all been classified according to their symmetry properties (*i.e.* the *body-fixed* reflection plane  $\hat{\sigma}_h$ )

Let us recall the electronic potential energy operator as constructed in section 1.2.3 [20].

$$\hat{V} = \hat{H}_{el} + \hat{H}_{SO} \quad \hat{H}_{el} = \hat{H}_{el}^0 + \hat{H}_{el}^1 \quad (2.31)$$

The first issue to deal with is the calculation of the *non-relativistic* electronic Hamiltonian  $\hat{H}_{el}$ . It was achieved using the software MOLPRO [46] for *ab initio* calculations (SA-CASSCF/MRCI in the VTZ-F12 basis) to obtain the *adiabatic* PES for the correlated to the corresponding asymptotic arrangements —  $\text{N}^+ (^3\text{P}_{J_A}) + \text{H}_2 (\text{X } ^1\Sigma_g^+)$  for the *reactant arrangement*, but  $\text{HN}^+ (\text{X } ^2\Pi_{\frac{3}{2},\frac{1}{2}}) + \text{H } (^2\text{S})$  and  $\text{HN}^+ (^4\Sigma^-) + \text{H } (^2\text{S})$  for the *product arrangement*. Note that from the eight total states converging to this last asymptotic arrangement, those corresponding to  $^5A''$  in the  $C_s$  group (*i.e.*  $^5\Sigma^-$ ) have been excluded on purpose. This is because they have repulsive potentials and hence their associated reaction channels are expected to be closed for the studied case.

The *product arrangement* has been treated with *adiabatic ab initio* calculations for the complete specification of the *adiabatic* spin-orbit states (8 correlated to the former asymptote, and 3 to the latter) — their couplings are ignored for the products.

Conversely, once the *adiabatic non-relativistic* PES of the *reactant arrangement* have been calculated — states  $1^3A''$ ,  $1^3A'$  and  $2^3A''$  in the  $C_s$  group (*i.e.* two  $^3\Pi$  and one  $^3\Sigma^-$  in the  $C_{\infty v}$  group) —, they are adapted to a preferable *diabatic* atomic basis  $|L_A\Lambda_A S_A \Sigma_A\rangle$ , which contemplates the non-adiabatic couplings between them [47].

$$\langle L_A\Lambda_A S_A \Sigma_A | \hat{H}_{el} | L_A\Lambda_A S_A \Sigma_A \rangle = \begin{pmatrix} E_{-1} & V_c & 0 \\ V_c & E_0 & V_c \\ 0 & V_c & E_1 \end{pmatrix} \quad (2.32)$$

Where, the already calculated *adiabatic* energies are just its eigenvalues.

$$E_1 = E_{-1} = E_{1^3A''} \quad (2.33)$$

$$E_0 = E_{1^3A''} + E_{2^3A''} - E_{1^3A'}$$

$$V_c = \sqrt{\frac{(E_{1^3A''} - E_{2^3A''})^2 - (E_1 - E_0)^2}{8}}$$

Although this diabatic representation is very useful, the chosen electronic basis was the *spin-orbit* adapted basis  $|J_A \Omega_A\rangle$ . Their relationship is mediated by the *3-j symbols* [19], which are mere generalizations of the *Clebsh-Gordan coefficients* in angular momentum coupling cases.

$$|J_A \Omega_A\rangle = \sum_{\Lambda, \Sigma} (-1)^{L_A - S_A + \Omega_A} \sqrt{2J_A + 1} \begin{pmatrix} L_A & S_A & J_A \\ \Lambda_A & \Sigma_A & -\Omega_A \end{pmatrix} |L_A \Lambda_A S_A \Sigma_A\rangle \quad (2.34)$$

Provided that the non-relativistic coupling term is slightly more complicated to study, it is expanded in a basis of spherical harmonics  $Y_{k\Lambda' - \Lambda}$ , so that the coefficients  $V_{\Lambda\Lambda'}^k$  in the diabatic basis set  $|L_A \Lambda_A S_A \Sigma_A\rangle$  are known.

$$\langle L_A \Lambda_A S_A \Sigma_A | \hat{H}_{el}^1 | L_A \Lambda_A S_A \Sigma_A \rangle = \delta_{\Sigma_A \Sigma'_A} \sum_k V_{\Lambda\Lambda'}^k(R, r) Y_{k\Lambda' - \Lambda}(\gamma, 0) \quad (2.35)$$

Applying the conversion into the original basis set, the final matrix elements are given by the following expression.

$$\begin{aligned} & \langle J\Omega' j' J'_A \Omega'_A p | \hat{H}_{el}^1 | J\Omega j J_A \Omega_A p \rangle = \delta_{\Omega\Omega'} c_{\Omega|\Omega_A - \Omega'_A|} \quad (2.36) \\ & \times \sum_{\Lambda, \Lambda'} \sum_{\Sigma} \sum_k (-1)^{k+j+j'+\Omega - \Omega'_A} V_{\Lambda\Lambda'}^k(R, r) \frac{\sqrt{[J_A][J'_A][k][j][j']}}{4\pi} \\ & \times \begin{pmatrix} L_A & S_A & J_A \\ \Lambda_A & \Sigma_A & -\Omega_A \end{pmatrix} \begin{pmatrix} L_A & S_A & J'_A \\ \Lambda'_A & \Sigma_A & -\Omega'_A \end{pmatrix} \begin{pmatrix} j & k & j' \\ 0 & 0 & 0 \end{pmatrix} \\ & \times \begin{pmatrix} j' & k & j \\ \Omega - \Omega'_A & \Omega'_A - \Omega_A & \Omega_A - \Omega \end{pmatrix} \end{aligned}$$

with

$$c_{\Omega|\Omega_A - \Omega'_A|} = \frac{\sqrt{2 - \delta_{\Omega 0} |\delta_{\Omega_A 0} - \delta_{\Omega'_A 0}|}}{2}$$

$$[J_A] \equiv 2J_A + 1 \quad [J'_A] \equiv 2J'_A + 1 \quad [k] \equiv 2k + 1 \quad [j] \equiv 2j + 1 \quad [j'] \equiv 2j' + 1$$

After introducing minor corrections like long-range interaction terms (*e.g.* charge-induced dipole, induced quadrupole), there is only left to find the spin-orbit interactions of  $\widehat{H}_{SO}$ . To do that, two reasonable assumptions were made: the *spin-orbit* coupling originates exclusively from the  $N^+$  cation, and it is considered to be constant through all the PES. Indeed, in the chosen *spin-orbit* adapted basis, this operator  $\langle J_A \Omega_A | \widehat{H}_{SO} | J_A \Omega_A \rangle$  is diagonal. Thus, the experimental spin-orbit splittings were taken from the NIST database [48].

After all, the central topic of this study is the dynamical study of the selected reaction, hence it is not worth to give further explanations about the construction of the potential energy surfaces. If one were interested in additional information regarding this specific topic, please go to the reference article by *Gómez-Carrasco et al.* [39].

## 2.3 Time-dependent validation

### 2.3.1 The 'Madwave3' program

Up to now, all the explained methodology corresponds to the dynamical study of the system in a *time-independent* fashion. Although this approach is completely legitimate by definition, there is no guarantee that the taken approximations (statistical capture method) hold properly for the case of study.

A proposed way to ensure the validity of the model is to compare the calculated results with those obtained with a more exact calculation. This is the case of the *time-dependent* approach, which is based on the propagation of a wavepacket  $\Psi(t)$  through the potential energy surface (PES) of the system by solving the *time-dependent Schrödinger equation* [49]. Since the wavepacket is not a stationary state in general, it is interpreted as a dynamical linear combination of eigenstates of the Hamiltonian  $\Phi_E$  (stationary states) — for the present dynamic calculations, these are actually continuum unbound eigenstates.

$$i\hbar \frac{\partial \Psi(t)}{\partial t} = \widehat{H} \Psi(t) \quad \Psi(t) = \int dE c(E) e^{-iEt/\hbar} \Phi_E \quad (2.37)$$

Using the Fourier transform (and its inverse), the time-dependent wavepacket is decomposed into its energy spectrum and the stationary eigenstates are thus found. This way, the final results obtained in the *time-dependent* approach are completely analogous to those based in *time-independent* perspectives.

The program used for the time-dependent validation is *Madwave3*, developed by *O. Roncero*. It applies the *time-dependent* approach for the modellization of three-atom reactions and estimation of reaction probabilities, among other features — for a complete description of the program, please refer to the source publication [50, 51].

Needless to mention that, as it is natural, the *time-dependent* approach also has its limitations (*i.e.* high computational cost), yet it is a *numerically exact* method. For this reason, this stage of the study is just devoted to have an initial qualitative comparison of results, using the simplified set of PES IV by *Nyman et al.* [12]

The propagation performed by *Madwave3* has a particularity which makes it different from an ordinary time propagation. The core of this approach consists in expanding the evolution operator  $e^{\frac{i\hat{H}t}{\hbar}}$  in  $T_k(\hat{H}, t)$  *Chebyshev polynomials* of degree  $k$  [37, 52].

$$e^{\frac{i\hat{H}t}{\hbar}} = \sum_k a_k T_k(\hat{H}, t) \quad \Psi(t) = \sum_k a_k \phi(k) \quad (2.38)$$

This kind of expansion is also applied to the time-dependent wavefunction  $\Psi(t)$ , ensuring a unique representation  $\phi(k)$  in terms of *Chebyshev* propagation steps [52]. It starts with  $\Psi(t = 0) = \phi(k = 0)$ , and then the rest of the propagation steps are recursively obtained by means of *Chebyshev* recurrence relations [52].

No further details will be provided in the present thesis, since the main point of using the *Madwave3* program is just for validation purposes — it is an intermediate tool, but not relevant by itself in this context. If one wanted to know more details about the *Madwave3* program, or the theoretical principles sustaining it, please go to the reference publication by *O. Roncero* [50, 51].

# Chapter 3

## Results and Discussion

### 3.1 One-dimensional problem

#### 3.1.1 Simulation parameters

As stated in section 2.1, the *effective potential*  $\mathcal{V}$  considered for the simplified model of the one-dimensional problem is an *Eckart potential* plus a *centrifugal barrier* originated from an angular momentum  $\ell$  — taken by convention as  $\ell = 20$  in this specific case.

$$\mathcal{V} = V + \frac{\hbar^2 \ell(\ell + 1)}{2\mu R^2} \quad (3.1)$$
$$V = V_0 \frac{-\xi}{1 - \xi} + V_b \frac{-\xi}{(1 - \xi)^2} \quad \xi \equiv -\exp\left(2\pi \frac{R - R_0}{L}\right)$$

The parameters of the *Eckart potential* have been chosen to emulate, as much as possible, a step potential ( $L \rightarrow 0$ ,  $V_b \rightarrow 0$ ). Keeping that in mind, the actual values of the parameters are, in atomic units,  $V_0 = 500 E_h$ ,  $V_b = 0.01 E_h$ ,  $R_0 = 1 a_0$ ,  $L = 0.05 a_0$ . As it is clear, the limit case which is intended to emulate — regardless the *centrifugal barrier* — with this set of parameters corresponds to a step potential of  $V_0 = 500 E_h$  centred at  $R_0 = 1 a_0$ . The discrete grid for the radial coordinate  $R$  has been defined between  $0.25 a_0$  and  $6.0 a_0$ , with a constant step  $\Delta R = 0.001 a_0$  — small enough to minimize numerical imprecision.

The numerical resolution of the *time-independent* Schrödinger equation was performed for a unit mass ( $\mu = 1 m_e$ ) with several values for the total energy  $E$ . As long as we are interested in the continuum unbound solutions, all the studied energies were taken above the asymptotic value of the potential step ( $E > V_0$ ).

### 3.1.2 Analysis of the wavefunction and resonances

The continuum unbound wavefunctions show sinusoidal patterns both in the real and imaginary parts, as it is expected for an incoming wave from the right asymptote to the barrier. Depending on the selected energy of the system, slight differences can be appreciated in the wavefunction.

When the total energy is below the effective potential barrier (Fig. 3.1), the wavefunction is not able to cross the barrier and remains in the right-hand side without falling into the step well — in accordance with the classical behaviour for a totally reflected particle unable to cross the potential barrier.

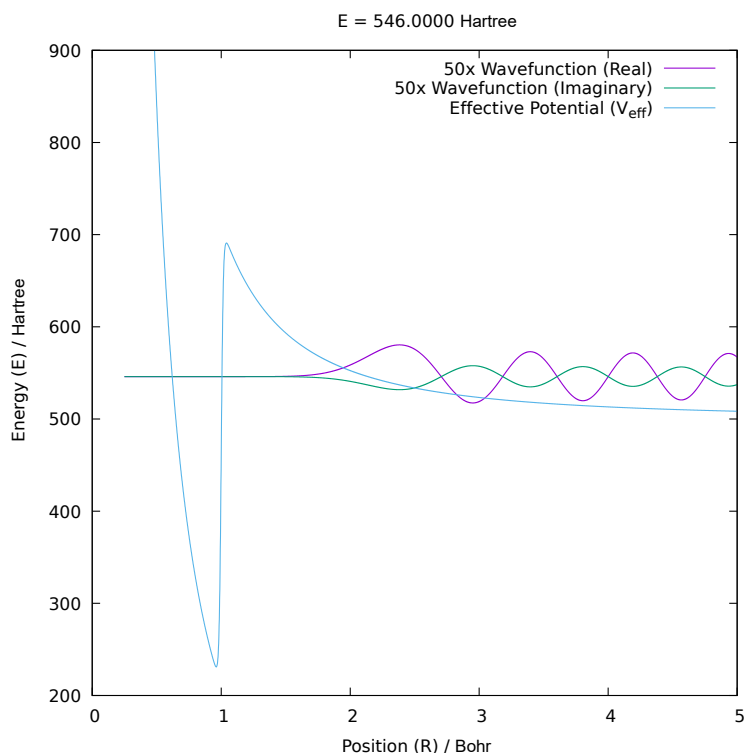


Figure 3.1: Ordinary behaviour of the unbound continuum wavefunctions for energies below the potential barrier. The amplitude has been increased a factor of 50 for a better visualization — arbitrarily centered at their corresponding energy value.

As the energy gets higher, the *tunnelling effect* [53] becomes more important, and the penetration of the barrier becomes more seizable, even allowing some non-negligible probability of crossing the barrier (Fig. 3.2).

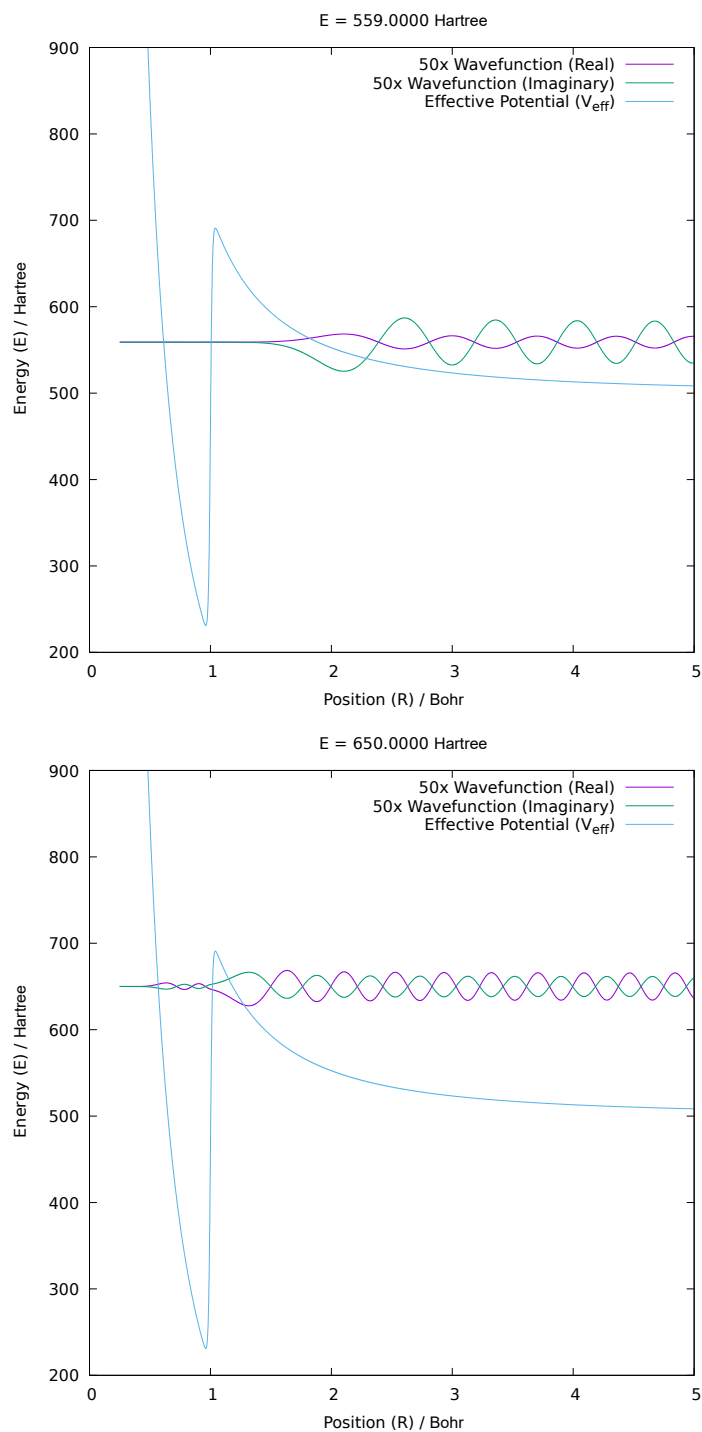


Figure 3.2: Illustration of tunnelling effect. The amplitude has been increased a factor of 50 for a better visualization — arbitrarily centered at their corresponding energy value.

Once the energy becomes higher than the barrier (Fig. 3.3), the system moves freely through all the available space, except for the infinite barrier at very short radial distances for which the wavefunction vanishes — arising from the centrifugal terms in the effective potential.

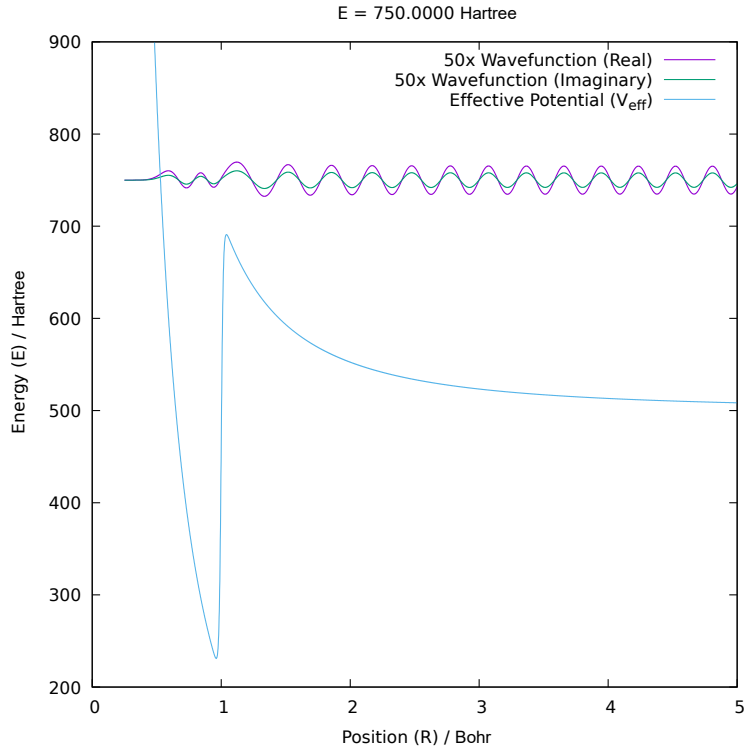


Figure 3.3: Ordinary behaviour of the unbound continuum wavefunctions for energies above the potential barrier. The amplitude has been increased a factor of 50 for a better visualization — arbitrarily centered at their corresponding energy value.

All the described cases correspond to the ordinary behaviour one may expect from the continuum unbound wavefunctions of the system. However, as it was introduced in previous sections, there are some specific energies for which the continuum unbound states are coupled to several bound states of lower energy — *i.e.* orbiting resonances. That is the case, for instance, at  $E \approx 557.2013 E_h$ , shown in Fig. 3.4.

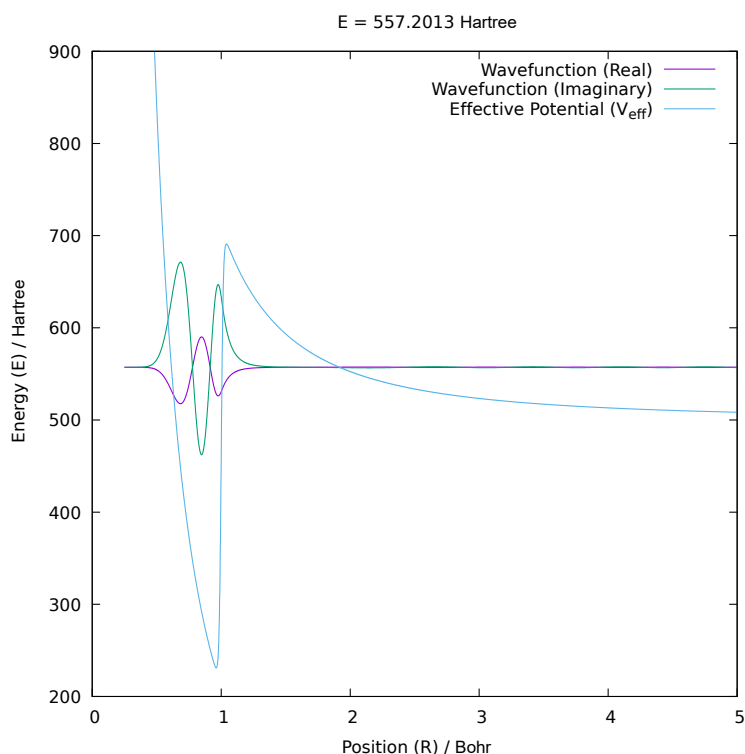


Figure 3.4: Resonant behaviour of the wavefunction at  $E \approx 557.2013 E_h$ . No scale factor has been introduced to the amplitude of the wavefunction — arbitrarily centered at their corresponding energy value.

The first interesting feature that is seen for the resonant wavefunction is that the amplitude is considerably bigger than the rest of the unbound states — around one order of magnitude bigger. This already indicates that this is not an ordinary solution.

Unlike the usual sinusoidal patterns at the right asymptote, the wavefunction is exclusively localized in the effective potential well and it does not extend outside that region — the wavefunction is 'trapped' in the potential well, and the barrier prevents it from escaping. Furthermore, both the real and imaginary parts of the wavefunction present a concrete number of crests, originating nodes between them (two nodes in this case). This resembles the well-known rovibrational wavefunctions of anharmonic one-dimensional molecular potentials (such as for the diatomic molecules), which would correspond to a vibrational quantum number  $v = 2$  function (two nodes) — though expected to appear at much lower energies.

In other words, at that specific energy, a resonance is coupling the continuum

solutions to the rovibrational bound state with  $v = 2$  — here is why this state is usually called a *quasi-bound state* [17].

The ultimate criterion for elucidating whether that state corresponds indeed to a resonance or not is the careful examination of the *scattering matrix*.

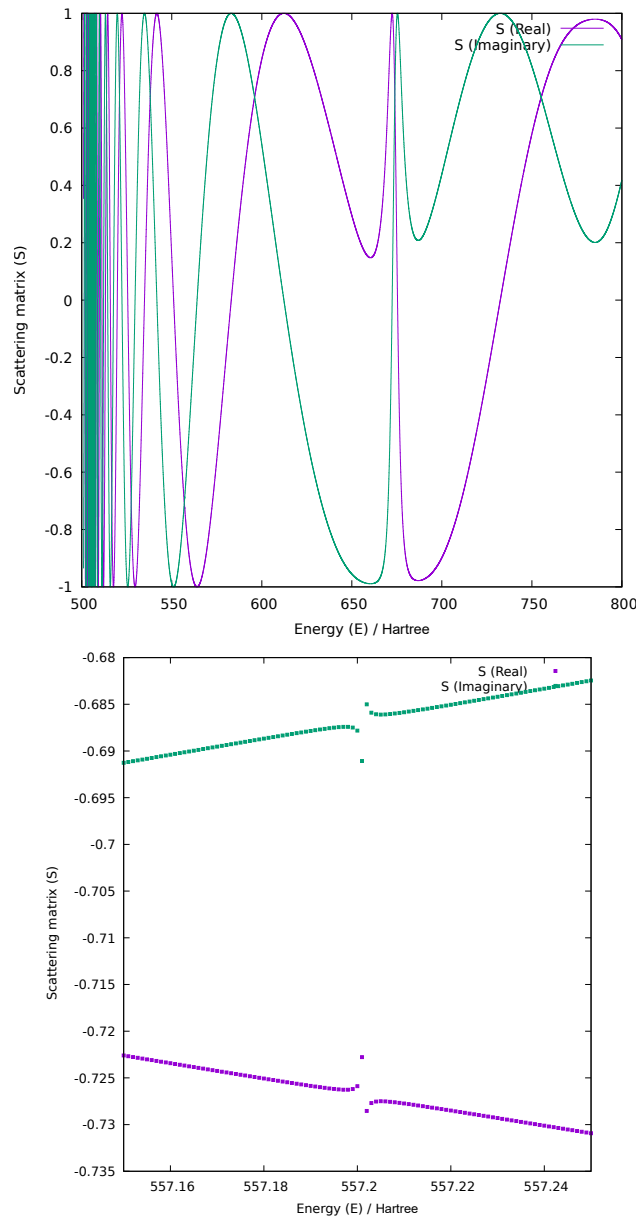


Figure 3.5: Real and Imaginary parts of the scattering matrix  $S$ , with a detail in the resonance region at  $E \approx 557.2013 E_h$ .

As it was mentioned in section 1.3.1, a resonance implies that there is a pole of the *scattering matrix* at that energy [30]. This is exactly what is observed in Fig. 3.5 at  $E \approx 557.2013 E_h$ , where there is a clear discontinuity in the real and imaginary parts.

Outside the exact energies where a resonance occurs, the *scattering matrix* is a smooth unitary function whose real and imaginary parts oscillate between 0 and  $\pm 1$  — so that the norm is held constant to the unity. Starting around  $500 E_h$  — the asymptotic right energy of the potential —, the oscillations are quite fast, but as the energy is increased, the fluctuations are gradually slowed — with wider crests and less frequent sign changes. This pattern is kept until the effective potential barrier is overcome around  $E \sim 670 E_h$ , when the wavefunction is no longer constrained by the barrier, and a significant change in its shape appears. Then, for even higher energies, the oscillatory patterns are recovered, slowly widening as before.

The analysis of the discontinuities in the *scattering matrix* is a useful way to elucidate the presence of resonances in the system. Unfortunately, it may be extremely hard if the resonance width is too small — such as in this case. For that reason, a more systematic alternative is applied to characterize not only its energy ( $E_r$ ), but also its half-width ( $\Gamma$ ) — as described in Ref. [17, 31].

This alternative method is based in the analysis of the overlap integrals  $\langle \Phi_v | \Phi_E \rangle$  between a bound state function  $\Phi_v$  ( $v = 2$  in this case), and the continuum solutions  $\Phi_E$  for all desired energies — or equivalently, for complex functions like these,  $|\langle \Phi_v | \Phi_E \rangle|^2$ .

As indicated in section 1.3.1, the resonance contribution to the *scattering matrix* is described by a quotient of the form  $\frac{iA}{E - E_r + i\Gamma}$ . Similarly, it can be shown that the overlap of the bound and unbound wavefunctions follow a *Lorentzian pattern*  $\mathcal{L}(E)$  [17, 31].

$$\mathcal{L}(E) = \frac{A}{(E - E_r)^2 + \Gamma^2} \quad (3.2)$$

Therefore, if the overlap data are fitted to the *Lorentzian distribution*, an accurate value of the energy ( $E_r$ ) and half-width ( $\Gamma$ ) of the resonance is obtained.

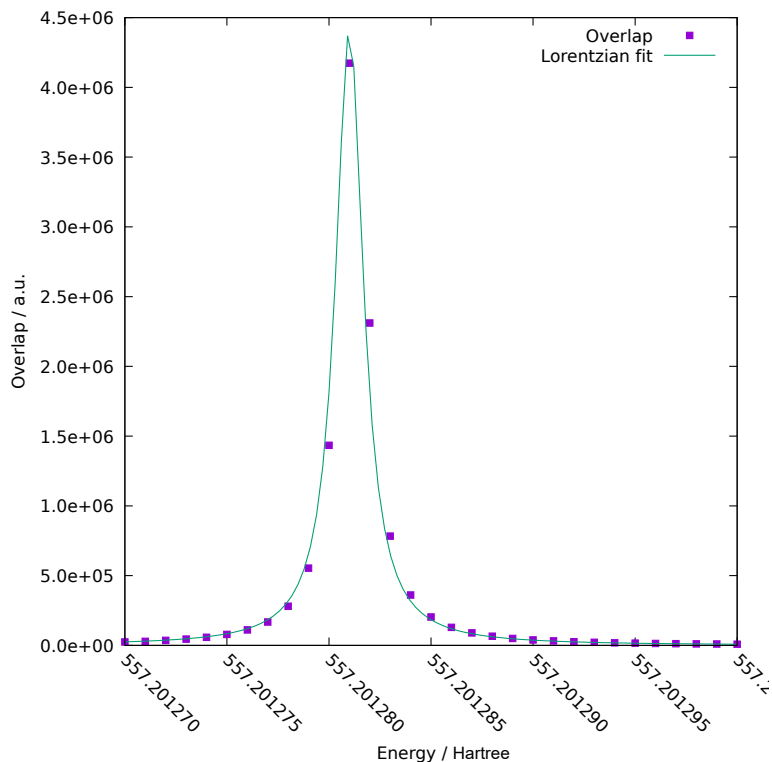


Figure 3.6: Overlap values of the bound  $v = 2$  function with the continuum solutions for each energy. The obtained Lorentzian fit parameters are  $A = 3.0730 \cdot 10^{-6} a.u.$ ,  $E_r = 557.2012812 a.u.$ ,  $\Gamma = 8.3370 \cdot 10^{-7} a.u.$

In view of Fig. 3.6, it can be said that the overlap results describe a *Lorentzian pattern*. The value of the fitted resonance energy  $E_r$  has been found at  $557.2012812 E_h$ , which perfectly matches the previous estimation of  $557.2013 E_h$ .

As for the resonance half-width, no wonder the fitted value is so small, as its characterization by the former method is a challenging task — it was first noticed when the energy resolution was augmented to the fourth decimal digit.

## 3.2 Time-dependent method validation

Now that the concept of *resonance* has been properly illustrated in the previous section by means of a simplified one-dimensional model problem, it is time to get back to the system of interest in this study — the reaction  $N^+ + H_2 \rightarrow NH^+ + H$ .

The first aspect to discuss is, as anticipated in section 2.3, how the results obtained by the *time-independent statistical* approach (central to this study) are compared with those obtained with a reference *time-dependent* method. Given the qualitative nature of this part of the study, the simpler potential energy surfaces by *Nyman et al.* [12] were used.

### 3.2.1 Simulation parameters

The simulation of the *time-dependent* method has been performed with the *Madwave3* program — developed by *O. Roncero* [50].

The same potential energy surfaces (*Nyman et al.* [12]) have been used in the *time-dependent* and *time-independent* calculations. The coordinates used in this last program are also Jacobi coordinates  $\{R, r, \gamma\}$ . Although the discrete grids for each coordinate are not exactly the same in both calculations, their differences are negligible for qualitative purposes like this.

The radial coordinate  $r$  is defined taking 512 points between 0.2 Å and 20 Å, while for  $R$  there are 768 points between 0.001 Å and 21 Å. The angular coordinate  $\gamma$  goes from 0 to  $\pi$  radians, taking 120 points. The initial wavepacket to propagate is a Gaussian wavepacket centered at  $r = 13.0$  Å with a mean energy of 0.35 eV, and a spreading of 0.2 eV.

The propagation starts from concrete reactant channels, and allowing the system to reach as many product channels as possible —  $j \leq 25$ ,  $v \leq 5$ . The entrance channel includes states from  $v = 0$  to  $v = 3$ , and from  $j = 0$  to  $j = 25$  — including the ' $p_d = \text{even}$ ' or ' $p_d = \text{odd}$ ' restrictions. The values of  $J$  and  $\Omega$  are tuned depending on the actual simulation conditions to reproduce.

As it will be shown in section 3.2.3, the validation of the statistical method has been performed for the case  $J = 0$ ,  $p = 0$ ,  $p_d = \text{even}$ . Despite their analogous nature, the employed basis are not exactly the same, as there are less restrictions on the simulated product channels in *Madwave3* [50]. Furthermore, the reactant channels simulated by *aZticc* [39] are restricted to  $j \leq 20$ ,  $v \leq 2$ , and not  $j \leq 25$ ,  $v \leq 3$ . The aim for this is mainly oriented to save computational resources and analyse the same statistical results in the following sections. As will be later demonstrated, the net effect of this truncation is not very drastic for these qualitative validations, and in fact the comparison between both methodologies is still perfectly achievable — see Fig. 3.8 of the next sections.

### 3.2.2 Time-dependent convergence

Although the *time-dependent* approach is a *numerically exact* method, the greatest issue of this kind of calculations is related to the actual convergence of the results. Only when full convergence is achieved, the results are truly reliable — non-converged results are not yet the final *numerically exact* outcomes of this method.

As it is shown in Fig. 3.7, the higher propagation steps are reached, the more converged is the obtained reaction probability — by definition, larger Chebyshev propagation steps are asymptotically proportional to larger simulation times [17]. For that reason, only once the convergence is achieved, a reliable result is found.

One interesting feature of the dynamical calculations is that, for the higher energies, the convergence is easier and faster than in the low energy range. This is natural, as a higher kinetic energy corresponds to a faster collisional process, and thus the reaction takes place sooner.

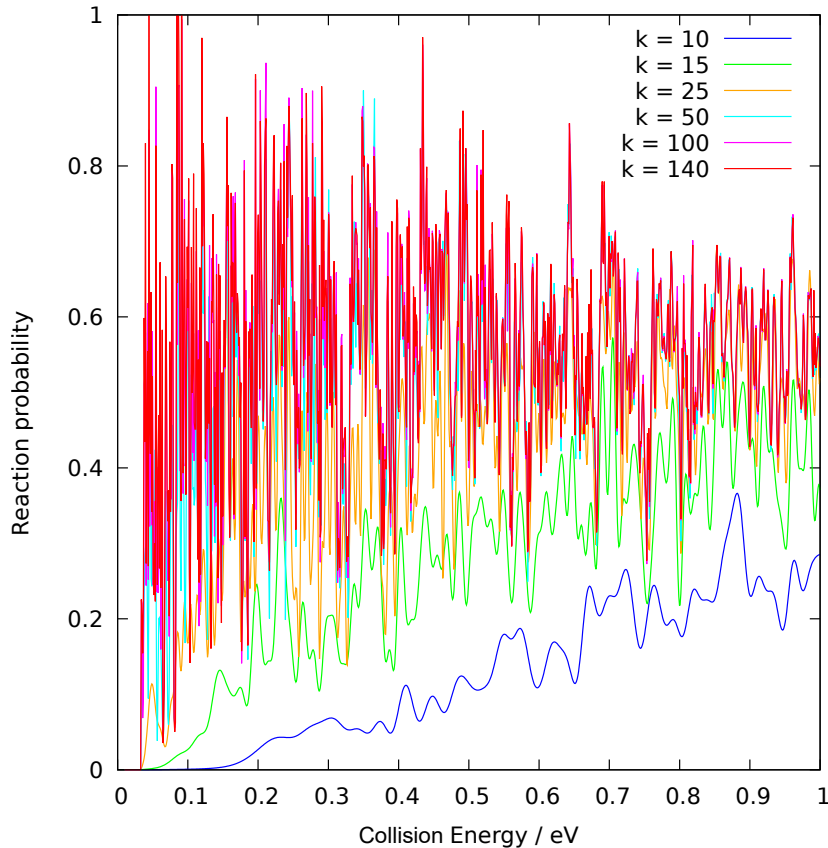


Figure 3.7: Convergence of the reaction probability calculated by Madwave3 for  $J = 0$ ,  $p = +1$ ,  $p_d = \text{even}$ . The Chebyshev propagation steps are labelled as  $k$ .

### 3.2.3 Validation of the statistical method

Assuming that all the calculations performed within the *time-dependent* approach are well converged — with minor numerical imprecision at lower energies as they need longer propagations and better absorption conditions (*i.e.* larger radial grids) —, their results act as a reliable reference to validate other methods. For this reason, from now on, the results of the *time-dependent* approach will be designated as 'exact'.

By definition of the statistical method, one may expect the reaction probability to be an average of the actual 'exact' results. The more statistically the reaction behaves, the more accurate the approximation. Following this idea, a hypothetical  $\text{NH}_2^+$  system with three equal masses — mass-analogous to

$\text{H}_3^+$  — was considered in both calculation approaches of this study — 'exact' and 'statistical'.

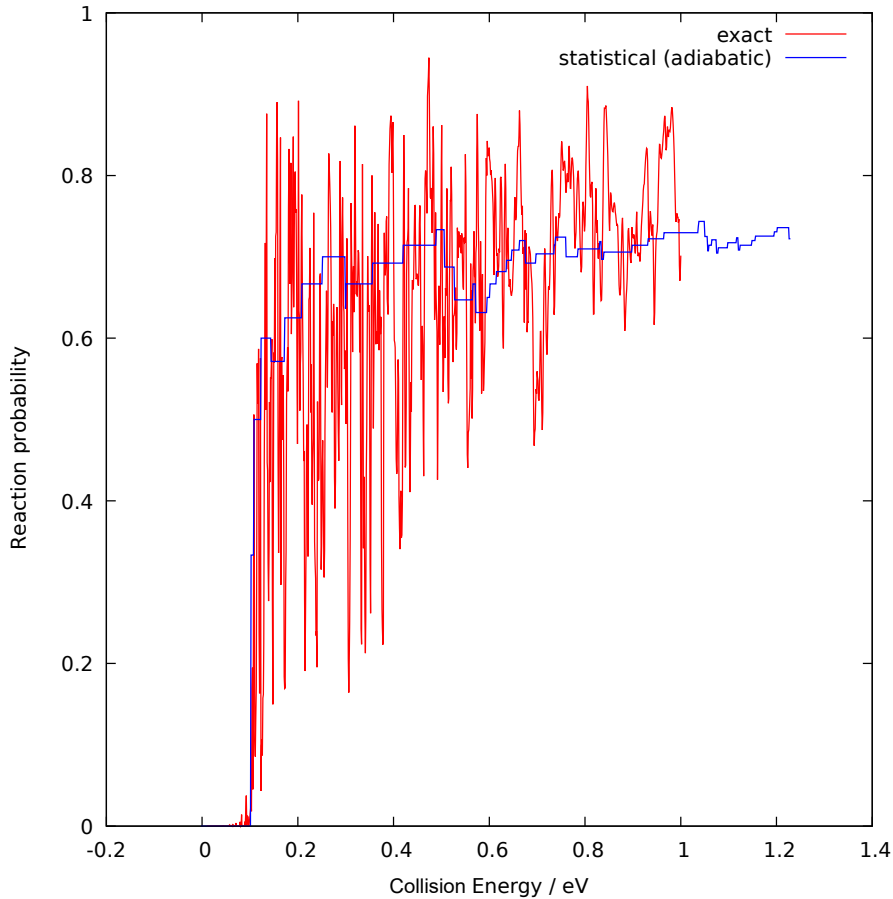


Figure 3.8: Comparison of the reaction probability calculated by Madwave3 [50] (red) and aZticc [39] (blue) for  $J = 0$ ,  $p = +1$ ,  $p_d = \text{even}$  (equal masses).

As it can be seen in Fig. 3.8, the statistical (adiabatic) results match really well to the average of the 'exact' reaction probability — *i.e.* the reaction behaves in a statistical way. This can be understood if we recall the requisites for a reaction to approach the statistical regime.

The potential energy surfaces of the system  $\text{NH}_2^+$ , as it has been mentioned before, present a deep well ( $> 6 \text{ eV}$ ) between the reactants ( $\text{H}_2 + \text{N}^+$ ) and products ( $\text{NH}^+ + \text{H}$ ) asymptotes — see Fig. 3.9 for an illustration of it. For not very high collision energies, when the system enters the well, it gets 'trapped' for a certain time. This long-lived reaction intermediate has 'lost'

its previous history, and thus it can finally exit through any of the available channels with no previous bias, which imposes a statistical behaviour.

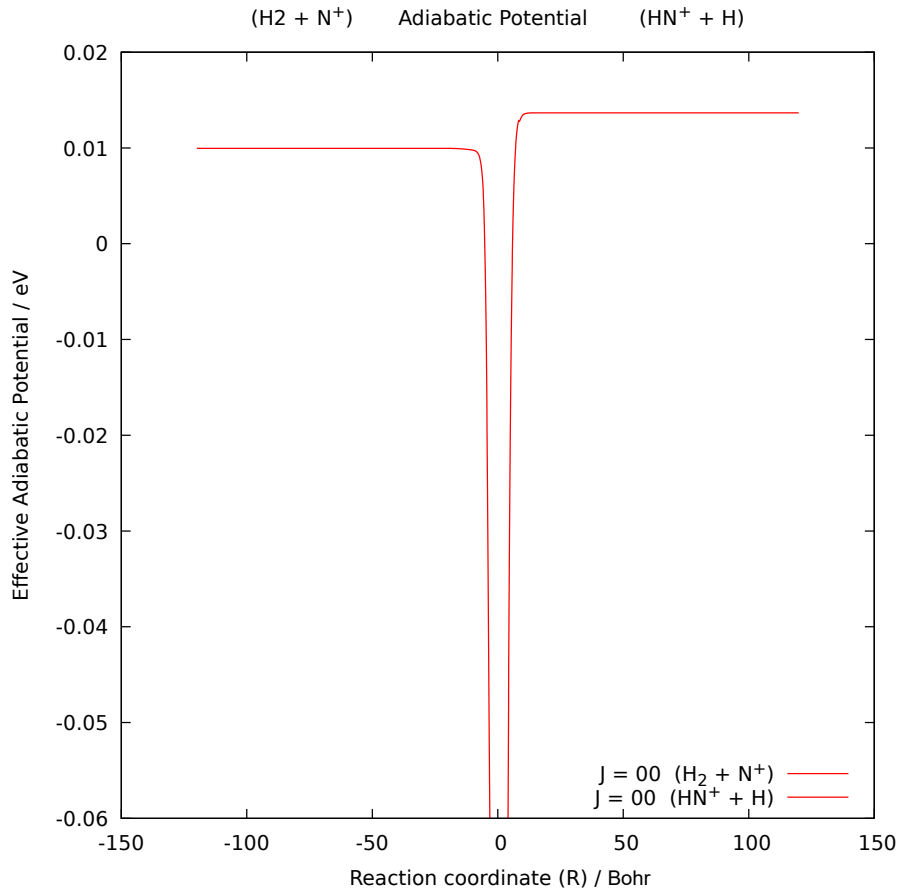


Figure 3.9: Adiabatic  $R$ -dependent potential energy curves for  $J = 0$ ,  $p = +1$ ,  $p_d = \text{even}$ ,  $j = 0$  (equal masses). They have been estimated by aZticc from the raw surfaces of *Nyman et al.* [12]

Going back to Fig. 3.8, a slight tendency could be observed regarding the energy ranges. Within the studied energy range, the agreement between both approaches is excellent — same threshold energy and overall evolution —. However, if really high energies would be considered, probably the results would deviate more and the model would become less accurate.

This is perfectly justified, since the long-lived reaction intermediate is only effectively formed if the system does not have very high collision energies. In case the reaction took place at really high energies, it is not likely that the

potential well could trap the system any more, and the intermediate complex would not last at all.

There is one additional consideration which is extremely important for the reaction to behave statistically. Up to now, the system has been taken as if the three atoms had the same mass, which suits perfectly for an equally statistical treatment for the three masses.

On the other hand, when the system has different masses, the statistical behaviour is expected to be less accurate due to the unequal bias introduced for each mass. This is why, for the real system of study  $\text{NH}_2^+$  (not equal masses), the results obtained by *aZticc* [39] do not match the 'exact' results as well as in the previous idealized case (Fig. 3.10).

The statistical approximation is no longer a perfect average of the 'exact' results, but still shows its main features, such as the same threshold, or the same overall shape — *i.e.* a similar distribution of channels being opened, as will be explained. For not very high energies, the approximation can be viewed as a not-so-bad choice, with just a slight tendency to overestimate the reaction probability — which may be later compensated by averaging over all the channels. Thus, for the lower energies, the statistical method gives reasonable results and it can be perfectly applied up to  $0.2 - 0.3 \text{ eV}$  — despite the reaction is still mediated by resonances even above that range.

Despite that the statistical approximation can still be reasonably applied for the system of this study  $\text{NH}_2^+$  (given its unique potential), this is not true in general for very different masses in presence of potential energy surfaces without very deep wells — *e.g.* this is reported by *Alexander et al.* [29] for the analogous system  $\text{OH}_2$ .

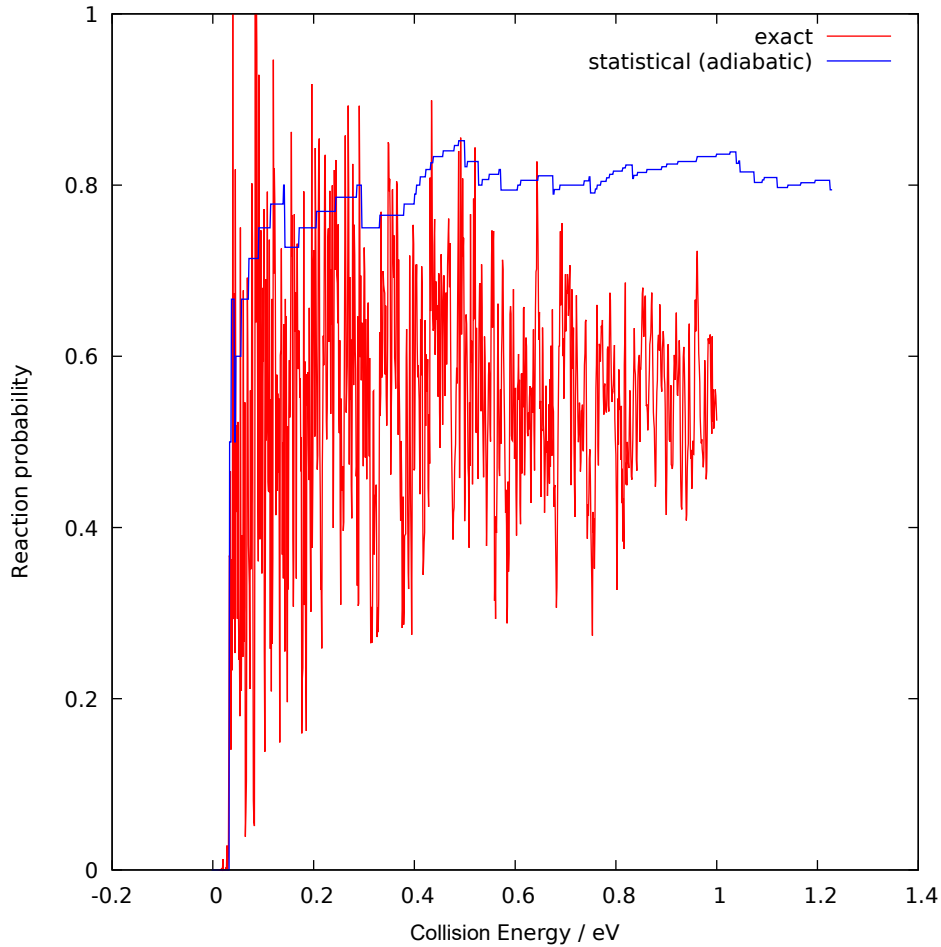


Figure 3.10: Comparison of the reaction probability calculated by Madwave3 [50] (red) and aZticc [39] (blue) for  $J = 0$ ,  $p = +1$ ,  $p_d = \text{even}$  (real masses).

The statistical method has been proven to be a valid approximation to properly model the reaction of interest in this study — assuming a certain error intrinsic to the method itself, but still not too high. Although at first sight one may prefer the *time-dependent* ‘exact’ methodology to avoid the inherent imprecision of the statistical approximation, there are plenty of reasons to rather use the latter.

Recalling what was said at the beginning of this section (3.2.2), the most hindering issue of the *time-dependent* methods is the problem of convergence. For these methods to give reliable results, the propagation times must be long enough to reach full convergence in all the selected energy ranges. In other words, the total calculation times can be extremely large, and can even

be unreachable in most cases — as for high total angular momenta  $J$ . The computational cost is definitely the main shortcoming of that approach, and is not a general cost-effective useful method except for a reduced number of conditions. For example, the actual calculations performed in this comparative study ( $J = 0$ ,  $p = +1$ ,  $p_d = \text{even}$ ) took around one month for the *time-dependent* propagation, but only a few minutes for the complete *time-independent* statistical method. Furthermore, at really low energies ( $1 - 10 \text{ meV}$ ), the *time-dependent* methods are extremely costly, since they require very long propagations and grids to ensure a proper description of the low linear momenta and adequate absorption regions [17, 50].

This is the main reason why, although the statistical approach is not absent of some imprecision, it is by far much cheaper than the 'exact' methods, and without great discrepancies in the final results.

What is more, there is even one additional feature about the statistical method which is not found for the 'exact' method. The reaction probability profile obtained with the statistical approach is characterized by several small discontinuities which rise or lower a little the probability. These correspond to previously closed channels which become open as the energy is increased, which are efficiently traced at each calculation step by the *aZticc* program. A detailed analysis of this will be covered in the next section (3.3.2).

### 3.3 Time-independent method

The general justification of the *time-independent* statistical method has been shown in the previous sections, where its main advantages and shortcomings are described. In this section, the results obtained with the *aZticc* program will be analysed, paying special attention to the effect which have the different magnitudes of the system on the results — using the simplified potentials by *Nyman et al.* [12]. Afterwards, a brief presentation of the final cross-sections and rate-constants will be shown — using the complete spin-orbit potential energy surfaces developed by the present research group [39].

#### 3.3.1 Simulation parameters

The simulation of the *time-independent* statistical method, as implemented in the *aZticc* program, calculates the capture probability of all the available channels, taking each arrangement separately —  $\text{H}_2 + \text{N}^+$  (reactant arrangement) and  $\text{NH}^+ + \text{H}$  (product arrangement).

It is worth to mention that although the *adiabatic* and *quantum capture* probabilities were calculated for both arrangements, the final *reaction probabilities* only consider the *adiabatic* capture of the products in the statistics — *i.e.* there are only pure *adiabatic-adiabatic* and mixed *quantum-adiabatic* results. The reason behind this concerns the small differences of both approaches compared to their unmatched computational cost — see the next sections for more details.

The real isotopic masses of each atom are taken ( $^1\text{H}$ ,  $^{14}\text{N}$ ), except for a few calculations oriented towards the analysis of their modification. These include the previously shown *equal-mass idealization*, and the replacement of hydrogen by deuterium.

All the energies considered in this study are referred to the bottom of the  $\text{H}_2$  potential energy surface, for which the reactant  $v = 0$ ,  $j = 0$  channel has an energy of  $2166 \text{ cm}^{-1}$ . This way, the energy range selected in this study corresponds to moderate energies between  $2166 \text{ cm}^{-1}$  ( $0.269 \text{ eV}$ ) and  $10311 \text{ cm}^{-1}$  ( $1.278 \text{ eV}$ ), with steps of  $5 \text{ cm}^{-1}$  ( $0.0006 \text{ eV}$ ). In this range the statistical approximation is expected to be acceptable — not very high energies. The diabatic basis has been truncated at  $15000 \text{ cm}^{-1}$  ( $1.86 \text{ eV}$ ), but its adiabatic counterpart is reduced to  $8000 \text{ cm}^{-1}$  ( $0.99 \text{ eV}$ ).

The system coordinates  $\{R, r, \gamma\}$  are discretized in optimal grids to fully cover the relevant regions of the simulated space — note that, as each arrangement is treated separately, the different definitions of the Jacobi coordinates are not a problem. The reaction coordinate  $R$  is divided in 6000 equidistant points from  $3 a_0$  to  $120 a_0$ , while the internal diatomic distance  $r$  takes 1000 equidistant points between  $0.3 a_0$  and  $2.8 a_0$ . For the angular coordinate  $\gamma$ , there are two grids depending on the calculated arrangement. For the product arrangement, 50 points between  $0$  and  $\pi$  radians were taken, while only 30 points between  $0$  and  $\frac{\pi}{2}$  because of the symmetry — *i.e.* 60 points between  $0$  and  $\pi$  radians.

The rest of the simulation parameters are related to quantum numbers of the basis functions, dependent on the specific calculations which are performed, and are tuned according to the desired conditions to emulate. There are some general trends which have been extensively used as a common reference for all the calculations presented in this study. For example, the electronic angular momenta of the atom are always set to  $L_A = 1$ ,  $S_A = 1$ , as the nitrogen atom is in the  $^3\text{P}_{J_A}$  state.

Unless otherwise stated, the upper truncation limits of the diatomic vibrational and rotational quantum numbers are also fixed to  $v = 0$  and  $j = 20$ , respectively. Of course, for the reactant arrangement, the hydrogen exchange parity  $p_d$  prunes the final values of  $j$  — considering either only even or odd values of  $j$ .

The last parameters to specify are the global parity  $p$  and the total angular momentum  $J$ , as well as the truncation of its projections  $\Omega$ . The values of  $J$  and  $p$  are taken for a broad variety of combinations, without any formal restriction other than an excessive computational cost. With respect to the projections  $\Omega$ , they are in general not truncated (*i.e.* from  $-J$  to  $J$ ) unless for preliminary convergence studies.

It is important to mention that the complete spin-orbit PES does take into account the values of  $J_A$  and  $\Omega_A$ , which are all contemplated in the *aZticc* program. However, for the single adiabatic PES by *Nyman et al.* [12], those values are no longer well-defined — nor  $L_A$ ,  $S_A$ . As this PES is only used to analyse the performance in all the calculations of section 3.3, the proposed solution in the *aZticc* program is to impose all the undefined values to zero when building the basis functions —  $J_A = 0$ ,  $\Omega_A = 0$  ( $L_A = 0$ ,  $S_A = 0$ ). Of course, this is not true in the reactant arrangement of real system  $\text{N}^+ (^3\text{P}_{J_A}) + \text{H}_2 (\text{X } ^1\Sigma_g^+)$ . In any case, it is not relevant just for these minor calculations as long as the correct simplified adiabatic potential is applied. Needless to say that the quantitative results obtained with the spin-orbit advanced PES do not suffer from this problem, as all the required quantum numbers are well-defined.

There are a few peculiarities regarding the symmetry of the basis functions which must be taken into account. This is the case, for instance, of the wavefunction associated to  $J = 0$ ,  $p = -1$ .

$$|J\Omega j J_A \Omega_A p\rangle = c_{\Omega\Omega_A} [|J\Omega j J_A \Omega_A\rangle + p(-1)^{J+J_A+L_A} |J - \Omega j J_A - \Omega_A\rangle] \quad (3.3)$$

In view of equation (3.3), it is clear that the wavefunction vanishes if the sign factor  $p(-1)^{J+J_A+L_A}$  gives a minus, and simultaneously the two non-adapted functions have the same value  $|J\Omega j J_A \Omega_A\rangle = |J - \Omega j J_A - \Omega_A\rangle$  — achieved when  $\Omega = 0$  and  $\Omega_A = 0$ .

Going back to the case when  $J = 0$  ( $\Omega_A = 0$ ), if we impose  $J_A = 0$  and  $L_A = 0$  (adiabatic simplified PES convention), the sign factor gives a minus, and hence that wavefunction is symmetry forbidden. Note that this restriction

only applies for the reactant arrangement and the mentioned conditions, as it is not present for the product arrangement or other calculations with  $J = 0$ ,  $p = -1$  but  $J_A \neq 0$ ,  $L_A \neq 0$  or  $\Omega_A \neq 0$ .

There are other peculiarities which also derive from this very principle, which have been observed in practical calculations too. For example, a generalization of the  $J = 0$  ( $p = -1$ ) anomaly occurs whenever there is  $J_A = 0$ ,  $L_A = 0$  and  $\Omega_A = 0$ . If  $J$  is an even number, then only  $p = +1$  is allowed under those conditions — and the opposite for odd  $J$  values.

### 3.3.2 Analysis of the open and closed channels

The simulation parameters have been presented in the previous section. Before going further in the different analysis of the results, it is time to explain in more detail the influence of opening and closing channels on the reaction probability.

Let us recall the previous reference case of  $\text{NH}_2^+$  (with its real masses), with  $J = 0$ ,  $p = +1$ ,  $p_d = \textit{even}$ . Since the vibrational quantum number has been constrained to  $v = 0$  for simplicity, the only magnitude which remains unspecified within each arrangement is the diatomic angular momentum  $j$ . It is precisely what characterizes the different asymptotic channels for this case, and their corresponding asymptotic energies are estimated by the aZtice program — as shown in Fig. 3.11. Truncating the basis up to  $j = 20$ , the total found channels are 8 for the *reactant arrangement* ( $j = 0, 2, 4 \dots$ ) and 21 for the *product arrangement* ( $j = 0, 1, 2, 3, 4 \dots$ ).

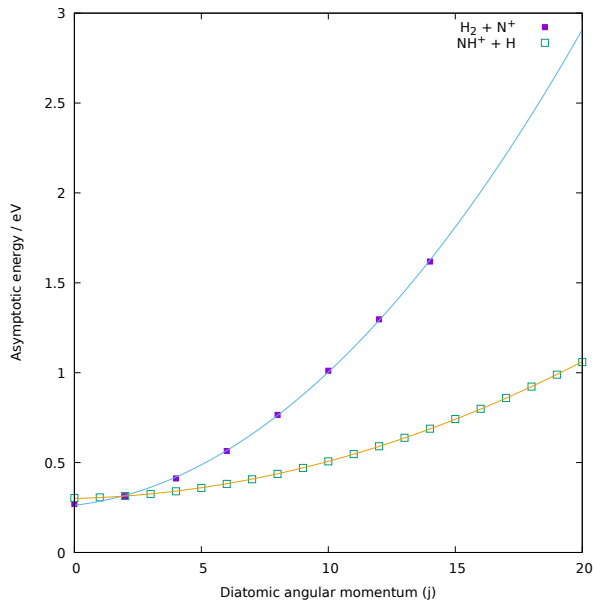


Figure 3.11: Asymptotic energies of the channels for each arrangement, corresponding to different values of  $j$ .

As a matter of curiosity, the energies of the channels within each arrangement describe a perfect parabolic distribution. This is because of the quadratic form of the kinetic energy terms associated to the angular momentum  $j$ , proportional to  $\frac{\hbar^2}{2\mu_{BC}r^2}j(j+1)$ . It can be easily checked by performing parabolic fits  $E \sim a_0 + a_1 j + a_2 j^2$  over the energy data, and focusing on the ratio of the  $a_2$  values —  $a_2 \sim 0.00582 \text{ eV}$  for reactants, and  $a_2 \sim 0.001738 \text{ eV}$  for products, so that their product/reactant ratio is around 0.30. This ratio should be equivalent to the quotient of the kinetic energy terms associated to  $j$ , approximating the variable  $r$  to the equilibrium geometry  $r_e$  of the two diatomic species —  $r_{e(H_2)} \sim 0.7414 \text{ \AA}$ ,  $r_{e(NH^+)} \sim 1.0362 \text{ \AA}$ , as published by the NIST [54].

$$\frac{\frac{\hbar^2}{2\mu_{NH^+}r_{e(NH^+)}^2}j(j+1)}{\frac{\hbar^2}{2\mu_{H_2}r_{e(H_2)}^2}j(j+1)} = \frac{\mu_{H_2}r_{e(H_2)}^2}{\mu_{NH^+}r_{e(NH^+)}^2} \sim 0.27 \quad (3.4)$$

As expected, the roughly estimated quotient agrees with the ratio of the fitted parabolic parameters, so the origin of the energy distribution of the channels is demonstrated.

Going back to the reaction probability, it is possible to rationalize the small 'jumps' of the probability in terms of the open and closed channels. Accord-

ing to the *adiabatic statistical* method, a channel is opened only when the total energy of the system can access that energy — so it is for the *quantum statistical* method, but with a smooth transition between being opened or closed. Hence, as the energy is gradually increased, more channels become open, and consequently a variation in the reaction probability is originated. If a formerly closed *product channel* opens, there is more chance that the system ends in the *product arrangement*, so the reaction probability increases. On the contrary, if the newly opened channel is a *reactant channel*, the reaction probability decreases.

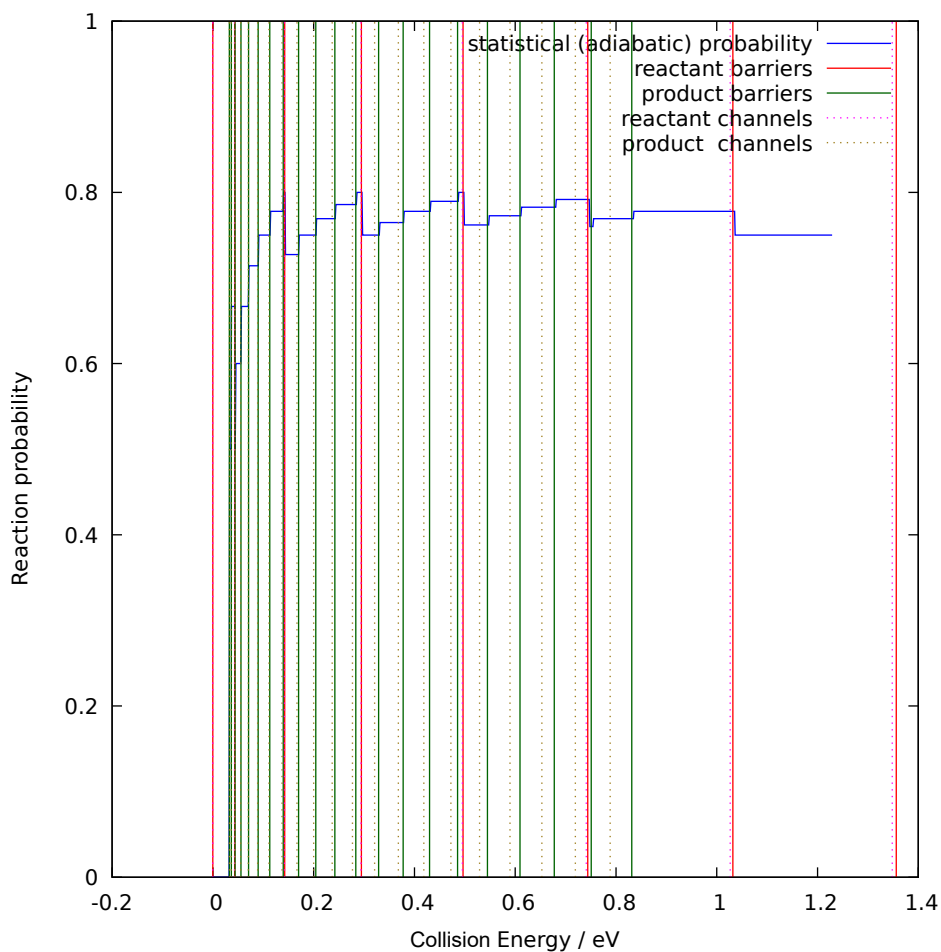


Figure 3.12: Correspondence between the fluctuations of the reaction probability (blue) and the opening of different channels (dotted green and red lines) — for  $J = 0$ ,  $p = +1$ ,  $p_d = \text{even}$  ( $j = 0$ ). The solid lines are the centrifugal barrier energies in the associated adiabatic potentials.

In view of Fig. 3.12, the influence of opening reactant and product channels is clear. For example, in the range below 1.2 eV, there are 7 of the total 8 modelled reactant channels which are opened in the end — being the first one always open. Their associated effect on the reaction probability is a consequent decrease, which are the 6 falls observed — the first reactant channel was opened before any of the product channels started to open. All the total 21 modelled product channels become opened in the end of the energy range below 1.2 eV, and thus 21 probability 'jumps' (increases) are found.

It is worth to mention that the channels of the product arrangement are closer in energy and less spaced than those of the reactants. This is not surprising, since the energies of the channels are inversely proportional to the reduced mass of the diatomic molecule as said above. As the molecule  $\text{NH}^+$  is more massive than  $\text{H}_2$ , the spacing for the product channels is expected to be smaller.

If the correspondence between the probability 'jumps' and the asymptotic energies of the channels is carefully analysed, one may realize that their agreement becomes worse as the channel energy is increased — *i.e.* higher values of  $j$ . This is completely normal, as any channel becomes opened when its centrifugal barrier is overcome, not when the asymptotic energy is surpassed. Hence, only for low  $j$  values, the barrier is small and the opening energy is almost the asymptotic energy.

### 3.3.3 Analysis of the capture probabilities

Although the reaction probabilities are the final desired result from the statistical method — the precursor for the *reaction cross-section* and the *rate constant* —, the actual primary outcomes of the calculations are the *capture probabilities*.

The *adiabatic* and *quantum* capture probabilities are similar to each other, but present small differences by construction, since the latter admits a gradual opening of the channels.

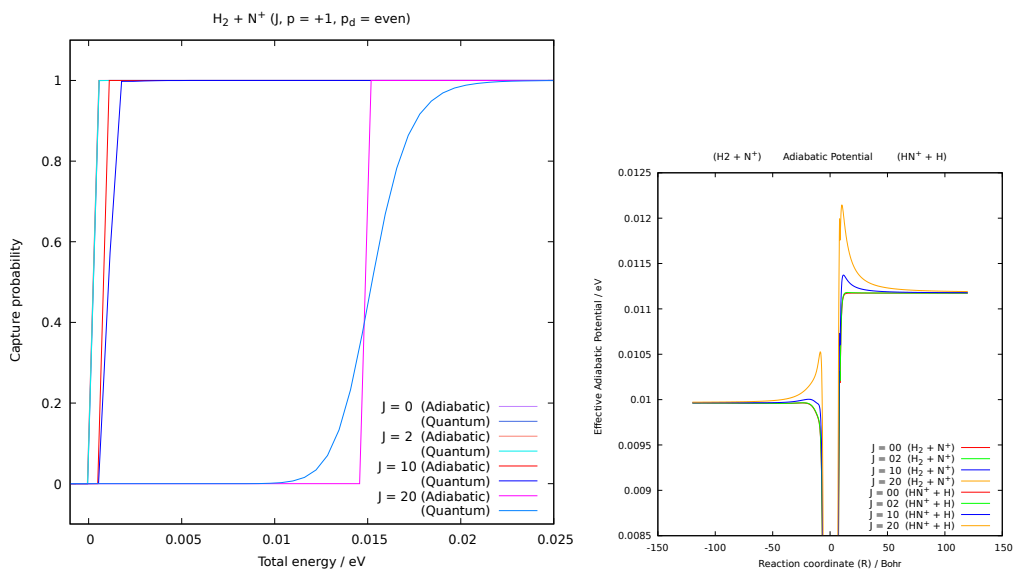


Figure 3.13: Adiabatic and Quantum capture probabilities for the reactant arrangement (left) and the adiabatic R-dependent effective potentials for both arrangements (right) —  $J = 0, 2, 10, 20$ ,  $p = +1$ ,  $p_d = \text{even}$ . Note that all the capture curves for  $J = 0$  and  $J = 2$  practically overlap.

As it is clear from Fig. 3.13 (left), the value of the total angular momentum  $J$  strongly affects the similarity between the *adiabatic* and *quantum* capture probabilities, as for  $J = 2$  they are practically the same, but for  $J = 20$  the differences are more obvious — the higher the angular momentum  $J$ , the greater differences between them. The justification for this can be found if the working potentials are carefully analysed — Fig. 3.13 (right).

The effective potential energy curves present the expected centrifugal barriers — higher barriers for higher values of  $J$ . As it was seen in the one-dimensional example, the presence of the centrifugal barriers facilitate the occurrence of *orbiting resonances* and *quasi-bound states*. They are only contemplated in the *quantum capture* model, but completely neglected for the *adiabatic model* — which only cares about the height barrier. For this reason, the greater the barrier, the more different the results of the two capture models are — note that  $J = 2$  is almost barrierless, yet  $J = 20$  has a very pronounced barrier.

The final reaction probabilities are, in consonance to the capture results, almost identical in the *adiabatic* and *quantum* approaches, as seen in Fig. 3.14 — there is slightly less agreement for  $J = 20$ .

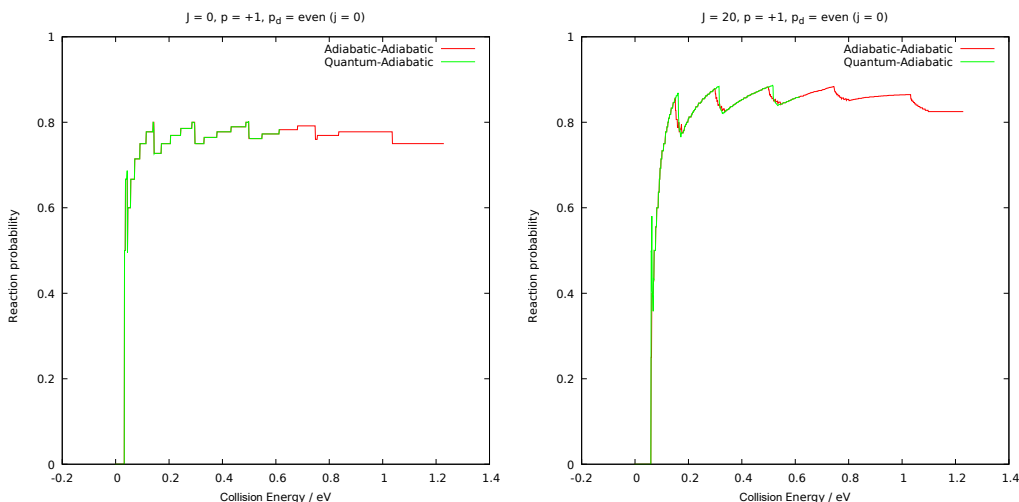


Figure 3.14: Comparison of the pure adiabatic and mixed quantum-adiabatic reaction probabilities for  $J = 0$  (left) and  $J = 20$  (right) —  $p = +1$ ,  $p_d = \text{even}$ . The product arrangement is always taken within the adiabatic approximation.

Given that the *adiabatic* and *quantum* probabilities are quite similar in many of the selected cases, most of the figures shown in this comparative study only show the *adiabatic* probabilities for the sake of simplicity and cleanness. However, for the real quantitative studies of *cross-sections* and *rate constants*, the *quantum* capture is always taken into account when needed — see section 3.3.7.

Note that the energy range for the *quantum* probabilities are shorter than their *adiabatic* counterparts, but the reason for this is quite simple. The *adiabatic* capture probabilities may extend indefinitely, as it becomes 1 for all energies above the opening threshold. Conversely, the *quantum* capture probability is only defined for a given effective energy range, which strongly depends on the available collisional energy. As the different entrance states have different energies, the final remaining energy employed in the collision is less than the original one. This is clear in Fig. 3.15, where the effect of increasing the quantum number  $j$  on the entrance state is explored. It is obvious that the last energies for which the quantum reaction probability is defined do indeed follow a quadratic distribution dependent on  $j$  — *i.e.* dependent on the energy loss at that level, proportional to  $j^2$  as usual.

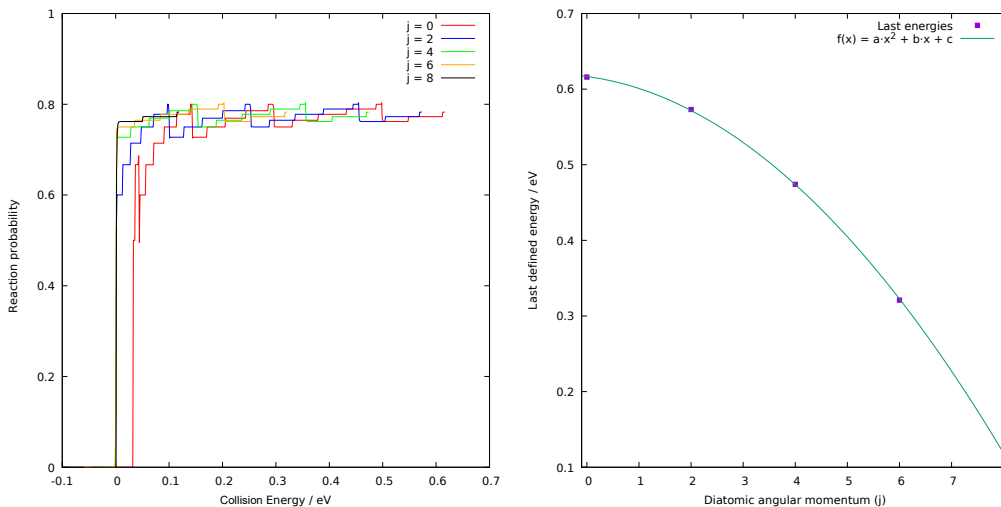


Figure 3.15: Comparison of the mixed quantum-adiabatic reaction probabilities (left) for different entrance states with increasing  $j$  values —  $J = 0$ ,  $p = +1$ ,  $p_d = \text{even}$ . Their last definition energies (right) are fitted to a parabolic function, with  $a = -0.0066 \text{ eV}$ ,  $b = -0.0092 \text{ eV}$  and  $c = 0.617 \text{ eV}$ .

Let us recall the capture probabilities at different values of  $J$  in Fig. 3.13 (left). One aspect that still has not been discussed is that the threshold energies are closer to each other as the total angular momentum  $J$  is decreased —  $J = 0$  and  $J = 2$  are practically overlapped. The explanation for this concrete distribution lies in the centrifugal terms of the Hamiltonian, with quadratic terms  $J(J + 1)$  — as well as others like  $-2\Omega^2$ . This quadratic distribution of the energies with  $J$  is perfectly reflected in the position of the capture thresholds.

### 3.3.4 Truncation of the ro-vibrational basis

One important issue to study is how important is the effect on the final results when the basis functions are truncated. In this section, the truncation of the ro-vibrational diatomic quantum numbers  $j$  and  $v$  is explored.

In view of Fig. 3.16, it is obvious that the less restrictive the truncation is, the more detailed is recovered in the final reaction probabilities. The more channels are simulated, the higher the overall probability gets, as there are more product channels being opened in the same energy range.

It is also possible to have an initial estimation of the energy range for which the different truncations are reliable. All the curves start following the same

path, but then at a certain energy, those with more severe truncations start to deviate from the rest — due to the absence of some channels that are present for the others. If the case for  $j \leq 20$  is taken as a reference, the first deviation energies are  $0.035 \text{ eV}$  ( $j \leq 0$ ),  $0.113 \text{ eV}$  ( $j \leq 5$ ),  $0.284 \text{ eV}$  ( $j \leq 10$ ) and  $0.548 \text{ eV}$  ( $j \leq 15$ ).

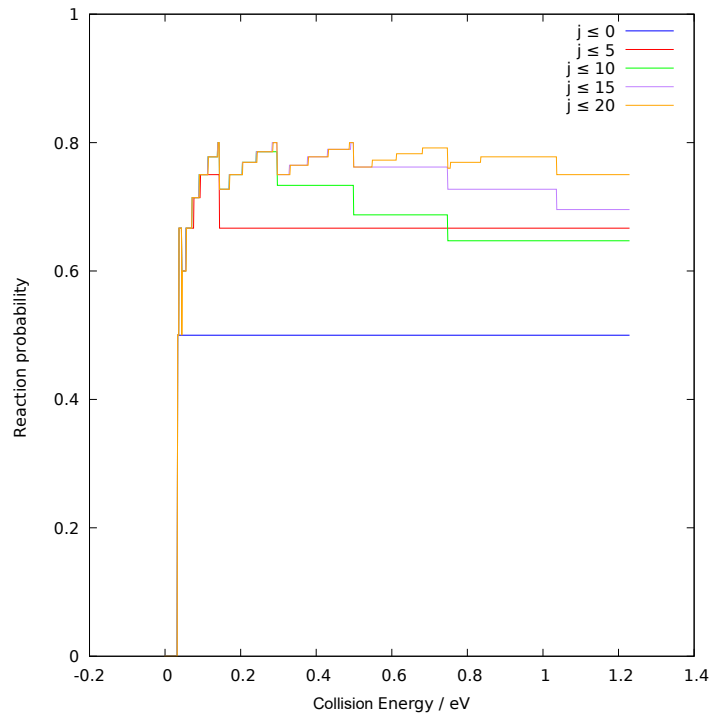


Figure 3.16: Comparison of the mixed quantum-adiabatic reaction probabilities for different truncations with increasing  $j$  values —  $J = 0$ ,  $p = +1$ ,  $p_d = \text{even}$ . The vibrational quantum number is always truncated to  $v \leq 0$

Let us now have a look on the truncation of the vibrational quantum number  $v$  — Fig. 3.17. As it was the case for the truncation of the rotational quantum number  $j$ , all the probability curves start together, but when a certain channel is absent for the stricter truncations, they take different directions.

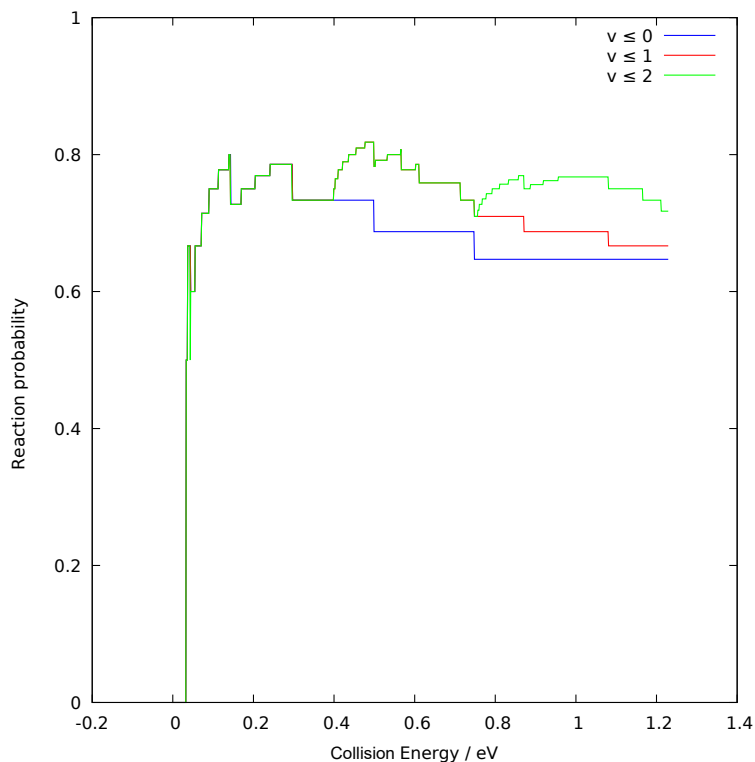


Figure 3.17: Comparison of the mixed quantum-adiabatic reaction probabilities for different truncations with increasing  $v$  values —  $J = 0$ ,  $p = +1$ ,  $p_d = \text{even}$ . The rotational quantum number is always truncated to  $j \leq 10$ .

In this case, as the diatomic vibrational states are more separated in energy, their opening becomes clearer when analysing the reaction probability — a significant curvature appears due to the multiple newly available ro-vibrational states. This takes place at energies  $0.394 \text{ eV}$  (opening of  $v = 1$ ), and  $0.756 \text{ eV}$  (opening of  $v = 2$ ). In fact, if it was intended to be a quantitative study, it seems reasonable to take  $v$  from 0 to 2 for the chosen energy range below  $1.2 \text{ eV}$  ( $v = 3$  remains closed in this range). However, as these kind of calculations are mere qualitative studies to analyse the performing of the statistical model, it will be limited to just  $v = 0$  — yet more states will be involved for the final quantitative studies in the last result section.

The final selected truncation for the validation calculations of this thesis has been set to  $j \leq 20$  and  $v \leq 0$ , unless otherwise indicated. It is reasonably big to cover most of the low-lying diatomic rotational states, but it still does not demand too much computational resources.

### 3.3.5 Truncation of the helicity

The projection of the total angular momentum  $\Omega$  — also known as *helicity* —, plays a fundamental role in the definition of the different channels. As it was mentioned in section 3.3.1, it can take integer values between  $-J$  and  $J$  — there are  $2J + 1$  possibilities. The problem with this arises when large values of  $J$  are considered, as the total number of channels becomes huge with an overwhelming computational cost.

Although the quantitative results of this study take all the possible values for more exactness, a reasonable choice would be to establish a truncation limit for the  $\Omega$  values in the simulation. For this reason, the effect of different truncations has been analysed for  $J = 20$ , setting the upper limit in absolute value to  $|\Omega| \leq 0, 5, 10, 20$ .

$\text{H}_2 + \text{N}^+ (p_d = \text{even})$					$\text{H}_2 + \text{N}^+ (p_d = \text{odd})$				
$ \Omega_{max} $	time / s	$n_{cl}$	$n_{op}$	$n_{tot}$	$ \Omega_{max} $	time / s	$n_{cl}$	$n_{op}$	$n_{tot}$
20	51881	28	36	64	20	72492	30	42	72
10	34174	22	36	58	10	42549	22	41	63
5	10676	12	27	39	5	13686	12	30	42
0	212	2	6	8	0	243	2	6	8

$\text{H}_2 + \text{N}^+ (\text{total})$					$\text{NH}^+ + \text{H}$				
$ \Omega_{max} $	time / s	$n_{cl}$	$n_{op}$	$n_{tot}$	$ \Omega_{max} $	time / s	$n_{cl}$	$n_{op}$	$n_{tot}$
20	124374	58	78	136	20	2588278	0	231	231
10	76724	44	77	121	10	886675	0	176	176
5	24362	24	57	81	5	210290	0	111	111
0	456	4	12	16	0	1655	0	21	21

Table 3.1: Comparative results for  $J = 20$ ,  $p = +1$  for different truncations  $|\Omega_{max}|$ . The CPU times are presented, along with the number of *open*  $n_{op}$ , *closed*  $n_{cl}$  and *total channels*  $n_{tot}$  at the highest simulated energy (1.278 eV).

As seen in table 3.1, the number of channels within a specific arrangement gets considerably decreased as the number of projections  $\Omega$  is reduced, as expected. Both the  $p_d = \text{even}$  and  $p_d = \text{odd}$  alternatives for the reactant channel have a similar tendency, so their mean behaviour can be directly analysed from their summed values —  $\text{H}_2 + \text{N}^+ (\text{total})$ .

In the reactant arrangement, the ratio between *open* and *closed channels* is slightly increased as the truncation is more severe — from  $\sim 57\%$  ( $|\Omega| \leq 20$ ) to  $\sim 75\%$  ( $|\Omega| \leq 0$ ) for the reactant arrangement. Although this tendency is

not observed for the product arrangement, all the simulated product channels are opened at that energy with all truncations — it is not possible to increase the open-channel ratio. The reason behind this predisposition towards the open channels for tighter truncations is not strange. When the number of total channels is pruned, the differences in number between open and closed channels become more relevant, as there are fewer options among which to choose. Equivalently, for a greater number of total channels, the small differences between open and closed channels are numerically attenuated in the division.

In order to have an objective criterion about the efficiency of the truncations, one possibility is to work in terms of relative magnitudes. As it is seen in Fig. 3.18, both the reactant and product arrangements have similar behaviours in terms of relative computation times and percentual recoveries of the total unpruned channels. Of course, we are only speaking about relative quantities, since the absolute number of channels is bigger for the product arrangement (as explained in previous sections), and so is its computational cost.

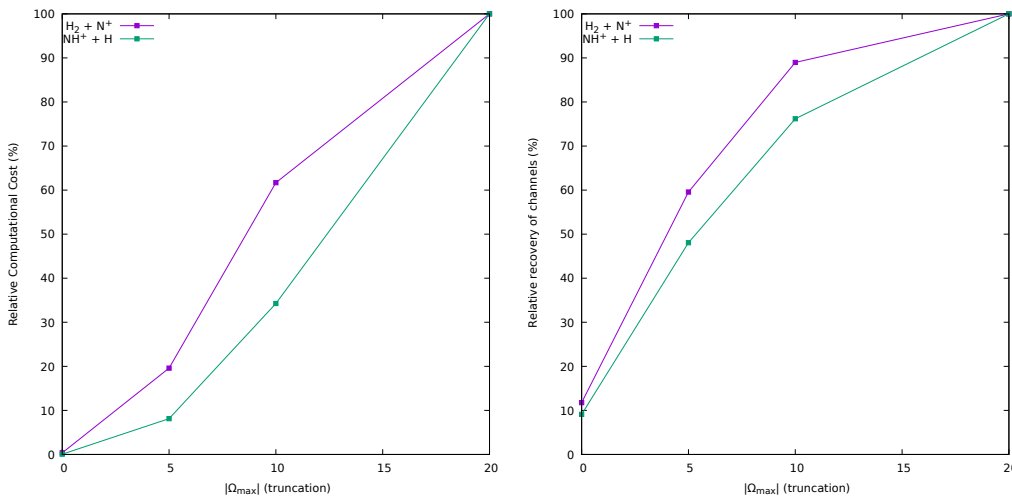


Figure 3.18: Relative computational cost (left) and percentual recovery of the total number of channels (right) for different truncations on the projections  $\Omega$  — for  $J = 20$ ,  $p = +1$ . The reference values are those obtained for the non-truncated calculations.

The relative evolution of the computational cost is reasonable as more projections  $\Omega$  are pruned, but the number of channels decreases more slowly. This is the case for the truncation  $|\Omega| \leq 10$ , which recovers more than 75% of the

channels with a huge decrease of the computational cost — up to 62% and 34% of the total cost, respectively for reactant and product arrangements.

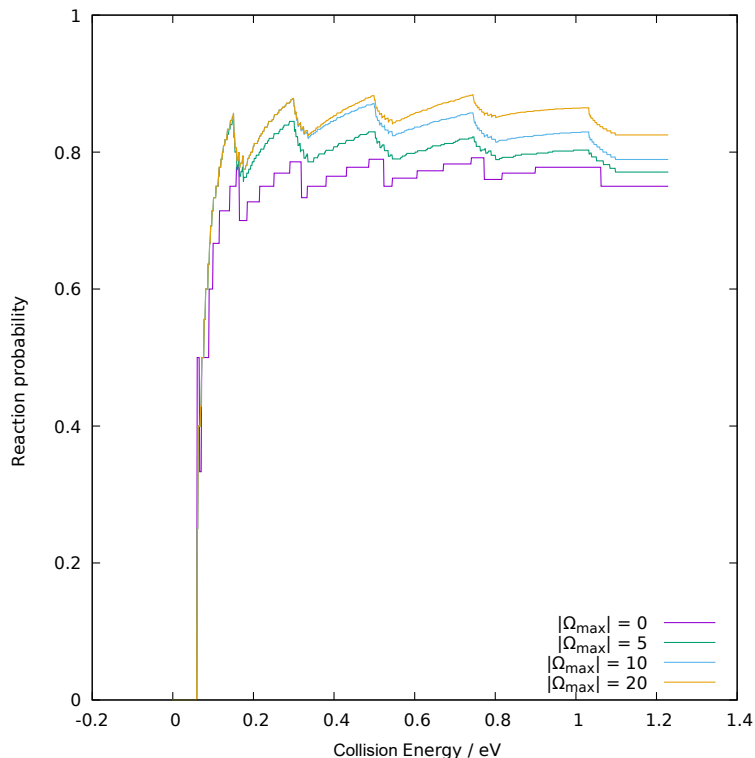


Figure 3.19: Effect of the truncation of projections  $\Omega$  on the reaction probability — for  $J = 20$ ,  $p = +1$ ,  $p_d = \text{even}$  ( $j = 0$ ).

One of the most important factors to take into account is the final effect of the truncation on the quality of the probability results. In view of Fig. 3.19, one can easily understand that the more restrictive the truncation is, the lower the quality of the final results — due to the pruning of the reactive channels considered. The greater the number of unpruned channels, the smoother the probability becomes, and its magnitude grows closer to the complete case.

The highest discrepancy between the truncated and the complete results occurs at the highest energies, as it is natural. Greater energies involve more open channels, which after all are the ones which originate the direct reaction mechanisms. For that reason, when some open channels are missing due to the pruning, their absence is more notorious for the final reaction probability. This also makes the convergence easier for lower energies, and hence less severe truncations last longer in good agreement with the complete

calculation. Consequently, the energies at which the probabilities start to differ correspond to the absence of an open channel absent for that pruning — *e.g.* at  $0.279\text{ eV}$ , the  $v = 0$ ,  $j = 11$  *product channel* opens, and since it is absent for  $|\Omega_{max}| \leq 10$ , a deviation from the  $|\Omega_{max}| \leq 20$  curve begins to appear.

The interesting conclusion to extract from this section is that, although the statistical method requires much less computational cost than a *time-dependent* complete calculation, it can be sometimes useful too to find a reasonable way to reduce the calculation times without compromising the quality of the results.

There is one more way for extreme cases when the computational cost is still unbearable. It consist in skipping the calculation of the quantum probabilities and just work with the adiabatic probabilities, since their magnitudes are really similar in most cases. However, this is discouraged because it is expected to give less accurate results *a priori* — see the final results of section 3.3.7.

### 3.3.6 Analysis of the mass

As it was shown at the early stages of this study, the masses of the atoms have a great impact on the accuracy of the statistical approximation — it dramatically affects many properties of the system. For this reason, it is worth to study the effect of the isotopic substitution of the hydrogen atoms for their deuterated analogues.

It is important to mention that, from a theoretical point of view, both  $\text{NHD}^+$  and  $\text{ND}_2^+$  are legitimate species to study. However, in order to keep the hydrogen exchange parity of the reactant arrangement, this section only focuses on the comparison of  $\text{NH}_2^+$  and  $\text{ND}_2^+$  — with analogous symmetry properties.

As seen in Fig. 3.20, the number of channels within the same energy range is considerably higher for the deuterated system. This is because the higher mass of the deuterium atoms make the energy levels to be closer in energy — and its *zero-point-energy* (ZPE) is lower too. Since there are more product channels with lower energies, the reaction threshold is slightly lowered too.

At first sight, one may conclude that the reaction probability of the deuterated system is partially decreased for the higher energy range. However, this is a consequence of the chosen truncation of the basis functions —

$j \leq 20, v \leq 0$ . In the ordinary hydrogenated system  $\text{NH}_2^+$ , there are fewer ro-vibrational levels in the high energy range, so the truncation is less aggressive for the final probability result.

On the other hand, the numerous levels of the deuterated system are severely affected by the truncation, specially with a significant loss of higher energy product channels. This implies that above  $0.5 \text{ eV}$ , only reactant channels are simulated and a fall appears in consequence — all the product channels within the truncation are already opened.

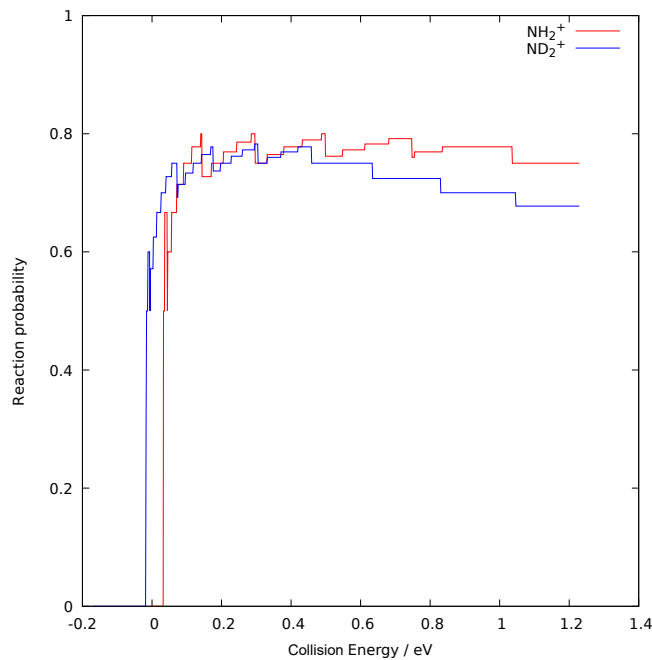


Figure 3.20: Effect of the deuteration on the reaction probability — for  $J = 0$ ,  $p = +1$ ,  $p_d = \text{even}$  ( $j = 0$ ). Note that the energy scale is conventionally referred to the non-deuterated reactant channel ( $\sim 0.269 \text{ eV}$ ).

Regardless the notorious differences due to the different isotopic masses of the hydrogen, it is also observed that, at least for the lower energy range, there are still some reminiscences in the evolution of the reaction probability for both cases — after all, they are analogous in most features (*e.g.* the symmetry properties).

### 3.3.7 Further application of the method

The aim of this final section is to provide a taste of the final *cross-section* and *rate-constant* results for the reaction of study. This is by no means a

detailed presentation of them, as they are fully covered and analysed in the upcoming publication *Gómez-Carrasco et al.* [39] by this research group.

As it was previously explained, for these quantitative results, detailed spin-orbit potential energy surfaces (PES) were developed for the reactant and product arrangements — the statistical approach does not require a description of the intermediate region with the deep well. The PES for the *reactant arrangement* explicitly treats the diabaticization of spin-orbit states, while for the *product arrangement* the adiabatic *ab-initio* spin-orbit states are directly taken.

The aZticc program was applied again with these new PES, imposing the following optimal simulation parameters — chosen for accurate but not too time-consuming calculations. The *reactant arrangement* was limited to  $v = 0$ , and  $j \leq 21$  — selecting only even or odd values depending on  $p_d$  —, yet for the *product arrangement*  $v \leq 1$ , and  $j \leq 30$ . Simulations with a total angular momentum from  $J = 0$  to  $J = 80$  were performed. In both cases, the upper bound for the total angular momentum projections was set to  $\Omega \leq 11$ . The studied energy interval ranges from  $0.26 \text{ eV}$  to  $0.85 \text{ eV}$ , in steps of  $0.5 \text{ meV}$ . The energy cutoff for the adiabatic-by-sectors basis was set to  $1 \text{ eV}$ .

Regarding the numerical resolution of the close-coupled equations, there is a subtle issue to take into account about the radial integration grid. Initially, 4000 equidistant grid points between  $R = 3 a_0$  and  $R = 80 a_0$ , which implies that the left asymptotic boundary conditions are imposed at  $3.0 a_0$  — *i.e.* the capture radius is  $R_c = 3.0 a_0$ . This criterion was also used through all the previous qualitative studies explained in this thesis.

During the optimization process for the quantitative study, among the different capture radii that were tried,  $R_c = 4.0 a_0$  had particularly interesting implications on the final results. For this reason, this alternative is also considered just for comparison.

The statistical models used for the quantitative work are the same as for the qualitative preliminary study, either pure *adiabatic-adiabatic* (AS) or mixed *quantum-adiabatic* (QAS) — designated as reactants-products. In the case of the mixed *quantum-adiabatic* approach, the results for  $R_c = 3.0 a_0$  and  $R_c = 4.0 a_0$  are presented for comparison, namely QAS<sub>3</sub> and QAS<sub>4</sub>, respectively.

As it can be seen in Fig. 3.21, the thermalised total cross-sections obtained with the mixed *quantum-adiabatic* method are always below the pure

*adiabatic-adiabatic* ones, since the adiabatic capture probabilities are always the unity once the potential barrier is surpassed — *i.e.* it systematically overestimates the reaction probability.

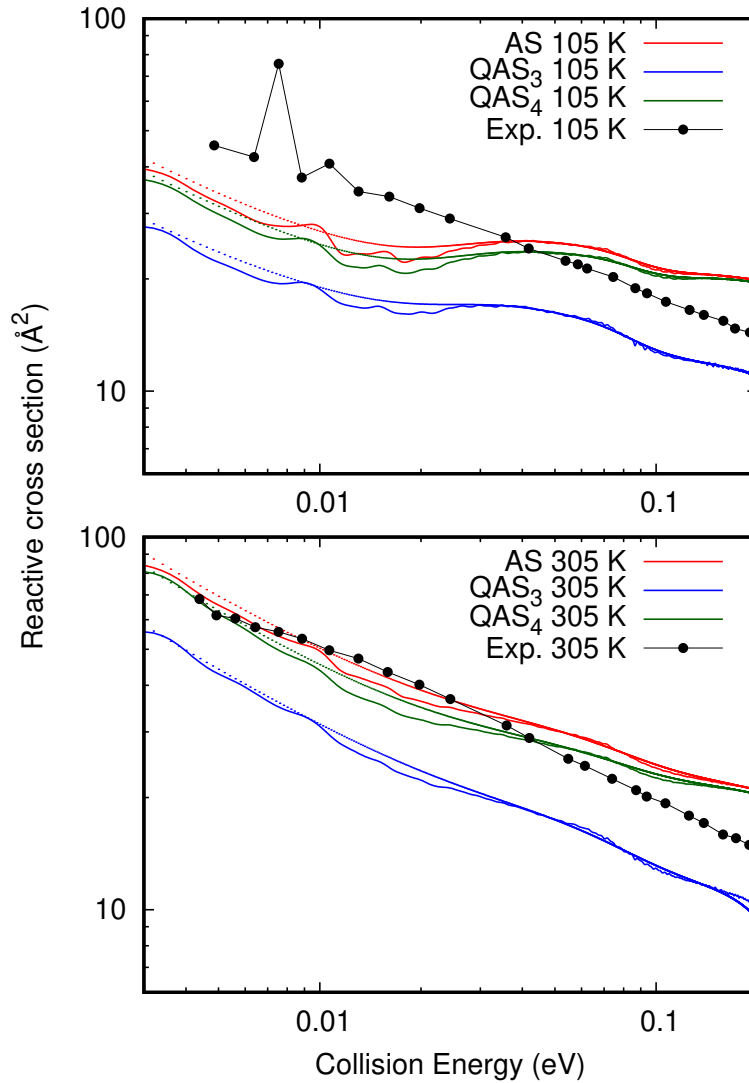


Figure 3.21: Thermal reactive cross-section at  $T = 105\text{ K}$  (up) and  $T = 305\text{ K}$  (down) for the adiabatic-adiabatic (AS) and quantum-adiabatic (QAS) models, along with the experimental results of Ref. [6]. The dotted lines are the convoluted results with *Doppler broadening* — as indicated by *Chantry* [55].

Unlike the simple case of only one electronic state, for multiple spin-orbit states like these the many quantum non-adiabatic effects become fundamental and the discrepancy with pure adiabatic models are more notorious — even more for higher energies.

In the energy range below  $0.03\text{ eV}$ , the purely adiabatic results (AS) seem to reproduce better the experimental data of Ref. [6]. Then, for higher energies, the adiabatic model overestimates the total reactive cross section and the actual experimental data are in between the results of the AS and QAS theoretical stimulations — being the results for  $R_c = 4 a_0$  the most suitable.

Although the mixed *quantum-adiabatic* results for  $R_c = 3 a_0$  are too low in the studied simulation conditions, it does not mean that they are inherently less accurate than the results for  $R_c = 4 a_0$ , or even the adiabatic ones. The fact that these last two methods give similar outcomes is only because the capture probabilities in those conditions are near to the unity in both cases — which leads to non-negligible overestimations at higher energies. Probably, if the product channel was treated in more detail like the reactant arrangement (*e.g.* non-adiabatic couplings), more balanced results would be obtained, but it is far beyond the scope of this work.

The effect of the temperature is also relevant, as the results for  $T = 305\text{ K}$  are better reproduced than those at the temperature of  $T = 105\text{ eV}$ , for which the estimated *cross-sections* are lower. Anyway, the experimental results have also certain degree of error due to the ion energy spread — specially for the lower energies. For this reason, other experimental sources should be checked as well, such as the rate-constant results by *Marquette et al.* [5] and *Zymak et al.* [7]

The most straight forward calculation of the thermal rate constants of the study assumes that the  $\text{H}_2$  species are pure ortho or para species. However, for the comparison with experimental results, mixtures of both species must be considered, for which the total ortho fraction  $f$  is taken into account while weighting the simulation results. For example, the natural n- $\text{H}_2$  corresponds to a fraction of  $f = 0.75$  (3:1 ratio). For simplicity, in this section the fractions  $f = 0.75$  and  $f = 0.005$  are shown in Fig. 3.22.

The agreement between the simulated and experimental rate constants is excellent. The QAS<sub>3</sub> model with reproduces best the results by *Zymak et al.* [7] with  $f = 0.005$ , and below  $50\text{ K}$ , for  $f = 0.75$  it lies between the experimental data from different sources — yet it is significantly lower for higher temperatures. Conversely, the AS and QAS<sub>4</sub> models are always in

between the different experimental data for the selected temperature range — QAS<sub>4</sub> is in general closer to the results by *Fanghanel et al* [8]. This is the most significant proof that the applied theoretical methods work properly for the quantitative modellization of the reaction — the ultimate objective of this thesis. For a complete discussion of the results, refer to *Gómez-Carrasco et al.* [39].

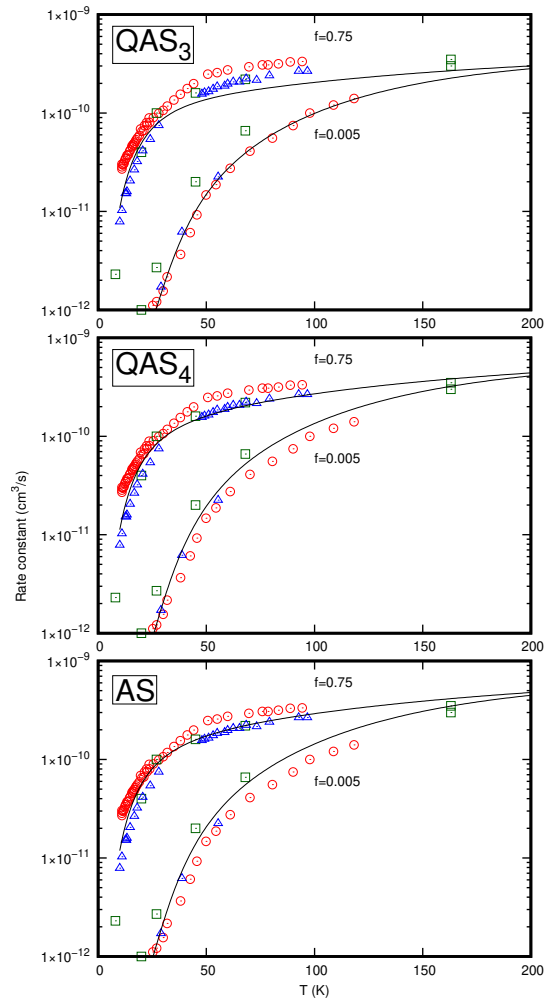


Figure 3.22: Thermal rate constants obtained within the three models for the two limiting experimental ortho fractions,  $f = 0.005$  and  $f = 0.75$  (n-H<sub>2</sub>). Symbol legend: circles (*Zymak et al.* [7]), squares (*Marquette et al.* [5]), triangles (*Fanghanel* [8]).

# Chapter 4

## Conclusions

The chosen nitrogen-containing insertion reaction has been studied in detail from a theoretical point of view. Starting from the basic concepts concerning coordinate definitions and the construction of the Hamiltonian operator, the formal derivation of reaction dynamics, *cross-sections* and *rate-constants* has been presented through this work.

The importance and main features of *resonances* have been analysed, from a simple one-dimensional model system, to the most advanced and sophisticated systems including *spin-orbit* couplings and *non-adiabatic* transitions.

The *time-independent close-coupling* method has been investigated as a suitable and reliable alternative to the popular *time-dependent* methodologies. For not very high energies and systems with similar characteristics to this one ( $\text{NH}_2^+$ ), the *statistical* approximation is a powerful way to obtain accurate results with a considerable decrease of computational costs.

The *adiabatic* and *quantum* statistical methods have been implemented and studied as reliable choices. In the case of only one *adiabatic* electronic state, the results obtained with the two approaches are quite similar to each other, and resonances become only significant when big centrifugal barriers are encountered. On the other hand, when multiple coupled *spin-orbit* states are considered, resonances become particularly important to the dynamics, since they can be seen as mediators for *non-adiabatic* transitions.

As a conclusion, a complete study of the statistical method has been successfully achieved, in the context of a real system of great relevance in astrochemistry. The initial objectives of this work are thus fulfilled.

# Bibliography

- [1] R. Le Gal, P. Hily-Blant, A. Faure, G. Pineau des Forêts, C. Rist, and S. Maret. “Interstellar chemistry of nitrogen hydrides in dark clouds”. *Astron. Astrophys.*, **562**:A83, 2013.
- [2] V. Wakelam, I. Smith, E. Herbst, J. Troe, W. Geppert, H. Linnartz, K. Öberg, E. Roueff, M. Agúndez, P. Pernot, H. M. Cuppen, J. C. Loison, and D. Talbi. “Reaction Networks for Interstellar Chemical Modelling: Improvements and Challenges”. *Space Sci. Rev.*, **156**:13, 2010.
- [3] A. C. Cheung, D. M. Rank, C. H. Townes, D. D. Thornton, and W. J. Welch. “Detection of NH<sub>3</sub> Molecules in the Interstellar Medium by Their Microwave Emission”. *Phys. Rev. Lett.*, **21**:1701, 1968.
- [4] P. Hily-Blant, G. Pineau des Forêts, A. Faure, R. Le Gal, and M. Padovani. “The CN/C<sup>15</sup>N isotopic ratio towards dark clouds”. *Astron. Astrophys.*, **557**:A65, 2013.
- [5] J. B. Marquette, C. Rebrion, and B. R. Rowe. “Reactions of N<sup>+</sup>(<sup>3</sup>P) ions with normal, para, and deuterated hydrogens at low temperatures”. *J. Chem. Phys.*, **89**:2041, 1988.
- [6] L. S. Sunderlin and P. B. Armentrout. “Rotational temperature dependence of the reactions of N<sup>+</sup> and C<sup>+</sup> with H<sub>2</sub>, HD, and D<sub>2</sub>”. *J. Chem. Phys.*, **100**:5639, 1994.
- [7] I. Zymak, M. Hejduk, D. Mulin, R. Plasil, J. Glosík, and D. Gerlich. “Low-temperature ion-trap studies of N<sup>+</sup>(<sup>3</sup>P<sub>*j*</sub>)+H<sub>2</sub>(*j*)→NH<sup>+</sup>+H”. *Astrophys. J.*, **768**:86, 2013.
- [8] S. Fanghaenel. “Low temperature collisions and reactions in a 22-pole ion trap”. *PhD thesis. Universität zu Köln*, 2018.

- [9] M. González, A. Aguilar, and Y. Fernández. “Analysis of the importance of the  ${}^3A_2$   $NH_2^+$  minimum in the ion—molecule reaction  $N^+ ({}^3P) + H_2 \rightarrow NH^+ + H$  by the quasi-classical trajectory method using a plausible single surface model”. *J. Chem. Phys.*, **104**(1):57–66, 1986.
- [10] M. González, A. Aguilar, and R. Sayós. “Low energy dynamics, isotopic effects and detailed microscopic reaction mechanism of the ion-molecule reaction  $N^+ ({}^3P) + H_2 \rightarrow NH^+ + H$ ”. *J. Chem. Phys.*, **132**(1-2):137–151, 1989.
- [11] U. Wilhelmsson and Nyman G. “A low energy quasiclassical trajectory study of  $N^+ + H_2$ ,  $N^+ + D_2$ . Dynamics, cross sections and rate constants”. *J. Chem. Phys.*, **96**:5198, 1992.
- [12] U. Wilhelmsson and Nyman G. “A low energy quasiclassical trajectory study of  $N^+ + H_2$ . Potential energy surface effects”. *J. Chem. Phys.*, **96**:1886, 1992.
- [13] C. L. Russell and D. E. Manolopoulos. “Time-dependent wave packet study of the  $N^+ + H_2$  reaction”. *J. Chem. Phys.*, **110**:177, 1999.
- [14] Z. Yang, S. Wang, J. Yuan, and M. Chen. “Neural network potential energy surface and dynamical isotope effects for the  $N^+({}^3P) + H_2 \rightarrow NH^+ + H$  reaction”. *Phys. Chem. Chem. Phys.*, **21**(40):22203–22214, 2019.
- [15] T. P. Grozdanov and R. McCarroll. “Statistical Theory of Low-Energy Reactive Collisions of  $N^+$  Ions with  $H_2$ ,  $D_2$ , and  $HD$  Molecules”. *J. Phys. Chem. A*, **119**(23):5988–5994, 2015.
- [16] T. P. Grozdanov, R. McCarroll, and E. Roueff. Reactions of the  $N^+({}^3P)$  ions with  $H_2$  and  $HD$  molecules at low temperatures. *Astron. Astrophys.*, **589**:A105, 2016.
- [17] O. Roncero. “*Simulaciones cuanticas en fisica molecular*”. Master de simulaciones en procesos moleculares. IFF (CSIC), 2010.
- [18] A. Lichnerowicz. “Elementos de cálculo tensorial”. *Aguilar*, 1972.
- [19] R. N. Zare. “*Angular Momentum*”. John Wiley & Sons, 1988.
- [20] C. Jouvet and J. A. Beswick. “Fine-structure electronic predissociation in van der Waals molecules. I. Theory”. *J. Chem. Phys.*, **86**(10):5500–5508, 1987.

- [21] C. Cohen-Tannoudji, B. Diu, and F. Laloe. “Quantum Mechanics”. *Wiley-VCH*, **1**:898, 1986.
- [22] D. A. Varshalovich, A. N. Moskalev, and V. K. Khersonskii. “*Quantum theory of angular momentum*”. World Scientific, 1988.
- [23] P. Atkins and J. de Paula. “Physical Chemistry”. *Oxford University Press*, **8**:798, 2006.
- [24] R. R. Reeves and P. Harteck. “Ortho and parahydrogen in interstellar material”. *Z. Naturforsch. A*, **34**(2):163–166, 1979.
- [25] D. W. Schwenke, D. G. Truhlar, and D. J. Kouri. “Propagation method for the solution of the arrangement-channel coupling equations for reactive scattering in three dimensions”. *J. Chem. Phys.*, **86**(5):2772–2786, 1987.
- [26] Edward J Rackham, Fermin Huarte-Larranaga, and David E Manolopoulos. “Coupled-channel statistical theory of the N (<sup>2</sup>D)+ H<sub>2</sub> and O (<sup>1</sup>D)+ H<sub>2</sub> insertion reactions”. *Chem. Phys. Lett.*, **343**(3-4):356–364, 2001.
- [27] E. J. Rackham, T. Gonzalez-Lezana, and D. E. Manolopoulos. “A rigorous test of the statistical model for atom–diatom insertion reactions”. *J. Chem. Phys.*, **119**(24):12895–12907, 2003.
- [28] M. Quack and J. Troe. “Complex formation in reactive and inelastic scattering: Statistical adiabatic channel model of unimolecular processes III”. *Ber. Bunsenges. Physik. Chem.*, **79**(2):170–183, 1975.
- [29] M. H. Alexander, E. J. Rackham, and D. E. Manolopoulos. “Product multiplet branching in the O (<sup>1</sup>D)+ H<sub>2</sub> → OH(<sup>2</sup>Π)+ H reaction”. *J. Chem. Phys.*, **121**(11):5221–5235, 2004.
- [30] W. H. Miller. “Study of the statistical model for molecular collisions”. *J. Chem. Phys.*, **52**(2):543–551, 1970.
- [31] A. Uma-Maheswari, P. Prema, S. Mahadevan, and C. S. Shastry. “Quasi-bound states, resonance tunnelling, and tunnelling times generated by twin symmetric barriers”. *Pramana*, **73**(6):969–988, 2009.
- [32] A. García-Vela. “Highly delocalized orbiting resonances”. *J. of Chem. Phys.*, **129**(9):094307, 2008.

- [33] M. Quack and J. Troe. “Specific rate constants of unimolecular processes II. Adiabatic channel model”. *Ber. Bunsenges. Physik. Chem.*, **78**(3):240–252, 1974.
- [34] J. Troe. “Statistical adiabatic channel model for ion–molecule capture processes”. *J. Chem. Phys.*, **87**(5):2773–2780, 1987.
- [35] T. González-Lezana. “Statistical quantum studies on insertion atom–diatom reactions”. *Int. Rev. Phys. Chem.*, **26**(1):29–91, 2007.
- [36] C. Eckart. “The penetration of a potential barrier by electrons”. *Phys. Rev.*, **35**(11):1303, 1930.
- [37] W. H. Press, S. A. Teukolsky, W. T. Vetterling, and B. P. Flannery. “*Numerical recipes 3rd edition: The art of scientific computing*”. Cambridge University Press, 2007.
- [38] M. Abramowitz and I. A. Stegun. “Handbook of Mathematical Functions with Formulas, Graphs, and Mathematical Tables”. *National Bureau of Standards Applied Mathematics*, **10**, 1972.
- [39] S. Gómez-Carrasco, D. Félix-González, A. Aguado, and O. Roncero. “Spin-orbit transitions in the  $N^+(^3P_{JA}) + H_2 \rightarrow NH^+(X^2\Pi, ^4\Sigma^-) + H(^2S)$  reaction, using adiabatic and mixed quantum-adiabatic statistical approaches”. *J. Chem. Phys.*, 2022.
- [40] O. Roncero, A. Aguado, and S. Gómez-Carrasco. “Radiative Processes in Astrophysical Molecules”. *IOP Publishing*, 2019.
- [41] F. X. Gadéa, H. Berriche, O. Roncero, P. Villarreal, and G. Delgado-Barrio. “Nonradiative lifetimes for LiH in the A state using adiabatic and diabatic schemes”. *J. Chem. Phys.*, **107**(24):10515–10522, 1997.
- [42] M. Metcalf and J. K. Reid. “*Fortran 90/95 explained*”. Oxford University Press, 1999.
- [43] B. R. Johnson and R. D. Levine. “A new approach to non-adiabatic transitions in collision theory”. *Chem. Phys. Lett.*, **13**(2):168–171, 1972.
- [44] B. C. Garrett, M. J. Redmon, D. G. Truhlar, and C. F. Melius. “A binomial treatment of electronically inelastic  $K + H$  collisions using a direct integration method for the solution of the coupled-channel scattering equations in electronically adiabatic representations”. *J. Chem. Phys.*, **74**(1):412–424, 1981.

- [45] B. Lepetit, J.-M. Launay, and M. Le Dourneuf. “Quantum study of electronically non-adiabatic collinear reactions. I. Hyperspherical description of the electronuclear dynamics”. *Chem. Phys.*, **106**(1):103–110, 1986.
- [46] H.-J. Werner, P. J. Knowles, F. R. Manby, J. A. Black, K. Doll, A. Heßelmann, D. Kats, A. Köhn, T. Korona, D. A. Kreplin, et al. “The Molpro quantum chemistry package”. *J. Chem. Phys.*, **152**(14):144107, 2020.
- [47] S. Gómez-Carrasco, A. Aguado, M. Paniagua, and O. Roncero. “Coupled diabatic potential energy surfaces for studying the nonadiabatic dynamics at conical intersections in angular resolved photodetachment simulations of  $\text{OHF}^- \rightarrow \text{OHF} + e^-$ ”. *J. Chem. Phys.*, **125**(16):164321, 2006.
- [48] NIST Chemistry Webbook. “<https://webbook.nist.gov/chemistry/>”. *National Institute of Standards and Technology*, 2022.
- [49] T. González-Lezana, A. Aguado, M. Paniagua, and O. Roncero. “Quantum approaches for the insertion dynamics of the  $\text{H}^+ + \text{D}_2$  and  $\text{D}^+ + \text{H}_2$  reactive collisions”. *J. Chem. Phys.*, **123**(19):194309, 2005.
- [50] O. Roncero. “Quantum wave packet program for triatomic systems”. <https://github.com/octavioroncero/madwave3>, 2021.
- [51] A. Zanchet, O. Roncero, T. González-Lezana, A. Rodríguez-López, A. Aguado, C. Sanz-Sanz, and S. Gomez-Carrasco. “Differential cross sections and product rotational polarization in  $\text{A} + \text{BC}$  reactions using wave packet methods:  $\text{H}^+ + \text{D}_2$  and  $\text{Li} + \text{HF}$  examples”. *J. Phys. Chem. A*, **113**(52):14488–14501, 2009.
- [52] H. Tal-Ezer and R. Kosloff. “An accurate and efficient scheme for propagating the time dependent Schrödinger equation”. *J. Chem. Phys.*, **81**(9):3967–3971, 1984.
- [53] Z. Ahmed. “Tunneling through a one-dimensional potential barrier”. *Phys. Rev. A*, **47**(6):4761, 1993.
- [54] R. D. Johnson III. “NIST. Computational chemistry comparison and benchmark database”. <https://cccbdb.nist.gov/>, **101**, 2022.
- [55] P. J. Chantry. “Doppler broadening in beam experiments”. *J. Chem. Phys.*, **55**(6):2746–2759, 1971.